TÜBİTAK

Turkish Journal of Physics

http://journals.tubitak.gov.tr/physics/

Invited Review Article

Turk J Phys
(2014) 38: 269 – 313

doi:10.3906/fiz-1407-23

Saga of efficiency degradation at high injection in InGaN light emitting diodes

Vitaliy AVRUTIN[1,*], Shopan A. HAFIZ[1], Fan ZHANG[1], Ümit ÖZGÜR[1], Enrico BELLOTTI[2], Francesco BERTAZZI[3], Michele GOANO[3], Arvydas MATULIONIS[4], Adam T. ROBERTS[5], Henry O. EVERITT[5], Hadis MORKOÇ[1]

[1]Department of Electrical and Computer Engineering, Virginia Commonwealth University, Richmond, VA, USA

[2]Department of Electrical and Computer Engineering, Boston University, Boston, MA, USA

[3]Department of Electronics and Telecommunications and IEIIT-CNR, Polytechnic University of Turin, Turin, Italy

[4]Semiconductor Physics Institute, Center for Physical Sciences and Technology, Vilnius, Lithuania

[5]US Army Aviation and Missile Research Development and Engineering Center (AMRDEC), Redstone Arsenal, AL, USA

Received: 23.07.2014 • **Accepted:** 24.07.2014 • **Published Online:** 10.11.2014 • **Printed:** 28.11.2014

Abstract: What has turned into highly complex and somewhat misunderstood efficiency loss mechanisms occurring in light-emitting diodes (LEDs) based on the InN-GaN material system at high injection levels are discussed. Suggestions are made as to the dominant mechanism(s) in an open forum format as well as pointing out some of the shortcomings of the methodologies used and premises forwarded. It is unequivocally known that increased junction temperature would cause a reduction in radiative power due to mainly the reduction in radiative recombination efficiency. Another obvious mechanism is the asymmetry in doping in wide bandgap semiconductors, such as GaN, wherein the hole concentration lags well behind that of electrons in the active region. Because an electron and a hole are required for radiative recombination, the radiative efficiency cannot keep up with increasing carrier injection due to progressively lagging hole population. This results in either electron escape without radiative recombination or electron accumulation, which in turn changes the internal bias of the device, manifested as reduced internal forward bias, which reduces the rate of increase in light intensity.

Some of the reports ascribe the efficiency loss at high injection levels to Auger recombination (mainly through indirect and recently reportedly direct deductions) as the main and or the only source of efficiency loss by in many cases simply relying on the temperature and injection *independent* (not well taken) A, B, C coefficients to fit a third order polynomial to the efficiency vs. injection current. As for the direct deduction, the spectroscopic analysis of Auger kicked hot electrons as they traverse through the Γ and L bands before being emitted into the vacuum by means of cesiated surface challenges the existing theories and some experiments regarding carrier scattering and Γ-L separation. Despite just a few reports to the contrary, the bulk of the resonant optical emission experiments do not support the Auger argument as being the main cause. In parallel, there exists a body of theoretical and experimental reports for electron overflow of ballistic/quasi-ballistic electrons traversing the active region to p-GaN, escaping recombination altogether in the active region. In fact and from the get go, the LED industry ubiquitously employed, and continues to do so, an (Al,In)GaN electron-blocking layer (EBL) to prevent electron escape for improved light output that in and of itself would more than suggest that the electron escape (overflow) does indeed occur. The only adverse effect of EBL is

*Correspondence: vavrutin@vcu.edu

that it impedes hole injection due to the valence band offset between the p-type (Al,In)GaN EBL and p-GaN and also generates piezoelectric (if not lattice matched) and differential spontaneous polarization induced fields that pull down the conduction band edge at the interface reducing EBL's effectiveness. To at least reduce the aforementioned aggravating factors to some extent, the electron overflow and the associated efficiency loss can be reduced substantially (particulars of which depend on the active layer design) by inserting a stair-case electron injector (SEI) with a step-like indium composition to act as an "electron cooler" or by linearly graded cooler in some form or another prior to the active region. Use of multiple layered heterostructures for the active layers also plays the role of electron cooler, albeit not necessarily in the most optimum fashion.

As if oblivious to the raging issues alluded to above, the LED industry has been moving along very successfully with a 2-prong approach. In one, dubbed the "high voltage LED", a set of LEDs (most likely configured in the form of a full-wave bridge rectifier) operating at low currents, where the efficiency is at its maximum, is used, which also has the added benefit of much reduced power supply complexity and weight. The other is the continual improvement of layer quality and optimum active layer design, taking technological parameters into consideration, which at the time of writing sported 63% wall-plug efficiency at an injection current of 350 mA for $\sim$1.1 mm $\times$ 1.1 mm LEDs, which translates to approximately 75% efficiency once the voltage (about 3 V) and phosphor conversion efficiencies are taken into account. Assuming the same extraction and external quantum efficiencies, one obtains about 86% for each. It would not be an exaggeration to conclude that mid 90% internal quantum efficiencies are very likely in play here, which means that the purported inherent problems dominating the discussion are practically reduced to an academic exercise. Despite aggravating factors involving holes and hetero-barriers, commercial LEDs almost invariably use multilayer heterostructure designs for the active layers, loosely termed as multiple quantum wells, presumably to circumvent technological challenges and the ramifications of the polarization induced field even though double heterojunction varieties could be preferable from the point of view of hole transport. Eventually, the real limiting factors are the extent of hole supply (can be mitigated by increased hole concentration, which is well known and continually explored) and the proverbial thermal wall (can be mitigated by increased efficiency and efficient heat removal) of course.

Key words: Light emitting diodes, III-nitrides, GaN, InGaN, efficiency droop, Auger recombination, carrier overflow

1. Introduction

Performance of InGaN-based light emitting diodes (LEDs) has improved considerably to the point where they are now penetrating the much coveted general lighting market. Lighting by LEDs is advantageous in terms of energy savings, environmental protection and safety, and long operation lifetimes. For high luminosity 2 approaches are explored. Namely one large area, often 1 $\times$ 1 mm^2, device operated at high injection levels (low voltage approach), and smaller sized multiple devices connected together (high voltage approach where LEDs are connected most likely in a full rectifier configuration) are being exploited. The latter has the added advantage of a much simpler powering scheme, which reduces cost and weight considerably. In the former approach, however, one pivotal problem, known as the efficiency degradation, i.e. lack of retention of the electroluminescence (EL) efficiency at high injection currents, has been a source of lively debate with no conversion in sight anytime soon [1–3]. This loss or retention manifests itself as the external quantum efficiency (EQE) reaching a peak value at relatively low current densities (as low as 1 A/cm^2), followed by a monotonic decrease observed under low duty cycle short pulsed current operation to rule out heating effects as its genesis [4]. It is essential to understand the physical mechanisms behind this degradation in efficiency and to eliminate it for helping to enable widespread use of LEDs in general lighting. The high voltage variety is made to operate where the efficiency is at its highest. Both large area (high current) and high voltage varieties are now able to produce over 250 lm/W efficiency with wall plug efficiencies, optical power divided by the electrical power, in excess

of 60% through improved quality and layer structural design, which is simply remarkable. One would then think that these performance metrics, which are not that far from the theoretical estimates considering all the efficiency terms involved, namely the voltage conversion ($\sim$90%), phosphor conversion ($\sim$90%), injection, and internal quantum efficiencies (articulated below), would suggest that an intrinsic killer process is not necessarily a dominant player here. However, obviously this is not shared across the board and the debate rages on even against the backdrops of impressive industrial LED performance.

Other unresolved issues involve the considerably smaller junction turn-on voltage than that expected and also the necessity to use a fraction, which varies wildly between 0.3 and 0.7, of the polarization charge one would expect, in simulations for consistency with experiments. Note that smaller than the expected turn-on voltage is not due to poor junction quality. Because of abundance of electrons in the system, one would surmise that the hole screening charge may not be in equilibrium, which plausibly may be the root cause of these apparent anomalies.

As alluded to in the already mentioned efficiency-retention problem, Auger recombination [5–9], polarization and bias-enhanced electron overflow [10–14] carrier delocalization, nonradiative recombination at defects, defect generation under high injection [15,16], and junction heating effects [17] have been proposed as possible causes for efficiency loss at high injection currents. To bring hot electrons into equilibrium with the lattice in LED active regions or at least cool them some, and thus reduce carrier overflow, a staircase electron injector (SEI) has been proposed and implemented [18]. The same can also be accomplished with linear or digital grading as well. Multiple quantum wells used for active layers also serve as electron coolers, albeit not as efficiently per se, due to band discontinuities not necessarily being equal to or more than one LO phonon energy. Clearly, none of the above mentioned effects can be ruled out entirely in the complex web of mechanisms taking place in LEDs at high injection levels, but the question before us really is which one or ones are dominant. Most of the studies exploring this problem considered either Auger recombination or the carrier overflow as the origin of the efficiency loss in InGaN LEDs, while the other proposed mechanisms are unlikely to be the primary cause although they may aggravate the problem (more details regarding the secondary possible mechanisms contributing to efficiency degradation can be found in a review article [19]). The current article critically reviews the plausible mechanisms attributed to the efficiency degradation in InGaN based LEDs.

2. A glossary of contributing factors to efficiency degradation

The junction temperature poses an intractable problem in regard to efficiency reduction in LEDs. This is due to the radiative recombination coefficient going down with increasing temperature and also any possible increase due to defect generation or new defect states being available for nonradiative recombination as the temperature is increased, both of which manifest themselves as reduction in internal efficiency. In addition, increased Joule losses cause reduction in the power conversion efficiency. The remedies include achieving higher efficiency through better material quality and efficient heat sinking.

The other ailments surrounding LED efficiency degradation involve current crowding, which can be assuaged by coating the surface with high conductivity transparent materials. The others involve nonradiative recombination induced by new defect generation and carrier delocalization allowing the manifold for access to a larger variety of defects. Another somewhat intractable contributor to loss is the asymmetry in electron and hole concentrations in the n- and p- sides of the junction. This problem is slowly but surely being mitigated by incremental improvements in the attainable free-hole concentration by growth optimization and structural optimization. The carrier overflow and Auger related efficiency loss will be discussed in some detail below.

The overall power conversion efficiency in an LED is the product of voltage conversion efficiency (first term in Eq. (1)), injection efficiency (portion of the injection current leading to carrier recombination over the total injection current, which accounts for carrier overflow) (second term in Eq. (1)), radiative efficiency (third term in Eq. (1)), and extraction efficiency (fourth term in Eq. (1)), and is given by

$$\eta_{wall-plug} = \frac{P_{out}}{VI} = \left(\frac{h\bar{\nu}}{qV}\right) \times \left(\frac{I_{active}}{I}\right) \times \left(\frac{P_{rad}/h\bar{\nu}}{I_{active}/q}\right) \times \left(\frac{P_{out}}{P_{rad}}\right) = \eta_{voltage} \times \eta_{inj} \times \eta_{radiative} \times \eta_{extraction}. \quad (1)$$

In the discussions that follow, we will be focusing on the product of radiative efficiency (internal quantum efficiency) and injection efficiency terms. The product of these represents the external quantum efficiency. Because of the ubiquitous use of the so-called ABC model for calculating and/or fitting the internal quantum efficiency, this particular model is discussed first.

2.1. A few words about the A B C coefficients

The rate equation for radiative and nonradiative processes applicable to LEDs (assuming no carrier overflow) is expressed as

$$-\frac{dn}{dt} = An + Bn^2 + Cn^3 - \left(G + \frac{\nabla J}{q}\right), \quad (2)$$

where n is the electron concentration, q is the elementary electron charge, and A, B, and C represent Shockley–Read–Hall nonradiative recombination coefficient, radiative recombination coefficient, and Auger recombination coefficient, respectively, in the units of s^{-1}, $\mathrm{cm}^3\ \mathrm{s}^{-1}$, and $\mathrm{cm}^6\ \mathrm{s}^{-1}$, respectively. The last term in the equation represents generation by e.g. optical excitation and or current injection if any. The implicit assumption is that all the carriers that are injected by current density J recombine either radiatively or nonradiatively in the active region. In the case of the carrier overflow or spill over depicting the case where the carrier traverse across the recombination region without recombining Eq. (2) is replaced with

$$-\frac{dn}{dt} = An + Bn^2 + Cn^3 - \left(G \text{ and or } \frac{\nabla J}{q}\right) + \nabla J_{spillover}/q. \quad (3)$$

It is critical to be familiar with the assumptions made to arrive at Eq. (3) as it is commonly used even when the assumptions made should preclude its use.

Regarding the A coefficient, which represents the Shockley–Read–Hall recombination, the actual rate equation governing the process is given by

$$U = \frac{\sigma v_{th} N_t (pn - n_i^2)}{n + p + 2n_i \cosh[(E_t - E_i)/kT]} = \frac{1}{\tau_{nr}} \frac{(pn - n_i^2)}{n + p + 2n_i \cosh[(E_t - E_i)/kT]}, \quad (4)$$

with the nonradiative rate or the inverse of nonradiative recombination time due to this event $\tau_{nr}^{-1} = \sigma v_{th} N_t$, which depicts the average lifetime of the minority carriers, where N_t is the trap concentration, σ is the capture cross section of the trap, v_{th} is the thermal velocity, p is the hole concentration, and n_i is the intrinsic carrier concentration.

If we assume that the trap energy level is $E_t = E_i$, one obtains $p_0 << n_0$, $n_i^2 << (p_0 + \Delta p)(n_0 + \Delta n)$, and $\Delta p \equiv \Delta n$, at high injection levels and or relatively low equilibrium electron concentrations $\Delta n > n_0$ (again

meaning $n = n_0 + \Delta n \simeq\approx \Delta n$ and $p = p_0 + \Delta p \approx \Delta p = \Delta n \approx n$ and $pn >> n_i^2$) Eq. (4) would reduce to

$$U = \frac{\Delta n}{2\tau_{nr}} = A\Delta n \text{ with } A = (2\tau_{nr})^{-1} \tag{5}$$

where n_0 and p_0 represent the equilibrium carrier concentrations, and Δn and Δp are the excess carrier concentrations.

Regarding the B coefficient for low excitation levels in a p-type semiconductor, the radiative recombination rate is expressed as

$$\frac{dn}{dt} = Bp_0\Delta n, \tag{6}$$

which at high excitation levels becomes

$$R = B\Delta n^2 \approx Bn^2. \tag{7}$$

Regarding the C coefficient, the particular variety of direct Auger recombination that applies to GaN based LEDs is mainly the *eeh* type in which case an electron from the conduction band drops to the valence band in that the energy given up by the recombining electron is transferred to another conduction electron, which is kicked higher up in the conduction band. The direct (i.e. phonon-less) Auger recombination coefficient is expected to decrease exponentially with the bandgap energy if the process involves transitions across the gap [20]. The applicable rate equation is given by

$$U_{Auger} = C_n\left[n\left(pn - n_i^2\right)\right] = C_n\left(n_0 + \Delta n\right)\left[\left(\left(p_0 + \Delta p\right)\left(n_0 + \Delta n\right) - n_i^2\right)\right]. \tag{8}$$

If $p_0 << n_0$, and $n_i^2 << \left(p_0 + \Delta p\right)\left(n_0 + \Delta n\right)$, i.e. the intrinsic carrier concentration n_i is very small, and if the injection rate is very high, i.e. the excess carrier concentration dominates over the equilibrium electron concentration, making the latter negligible, Eq. (8) can be rewritten as

$$C_n\left(\Delta n\right)^3 \approx C_n n^3 \tag{9}$$

Clearly, as articulated above, there are myriads of assumptions made to arrive at the rate equation

$$U = -\frac{dn}{dt} = An + Bn^2 + Cn^3, \tag{10}$$

which is commonly used to infer the presence and in fact dominance of Auger recombination and extract a C coefficient. To reiterate, it is under the erroneous assumptions that $(i) A, B$, and C coefficients are temperature, design, and injection level independent, and (ii) there is no carrier overflow (leakage current).

2.2. Experimentally determined and calculated Auger coefficient, C

Pathways to Auger recombination are many but include the direct Auger recombination, such as the *eeh* variety (Figure 1, left panel) in which the energy given off by an electron dropping to the valence band from the conduction band is consumed to excite another conduction band electron to higher states in the conduction band all the while satisfying energy and momentum conservations. The likelihood of the *hhe* process in the valence band is some one tenth that of the *eeh* process and can thus be ignored as well as the other direct Auger processes. The indirect Auger recombination, which can occur in parallel to the direct variety, encompasses phonon-assisted processes and/or many other scattering mechanisms (Figure 1, right panel). Naturally, therefore, the indirect Auger process gets to be very complex to untangle and exhibits a power law dependence on temperature unlike the direct variety, which depends exponentially on temperature.

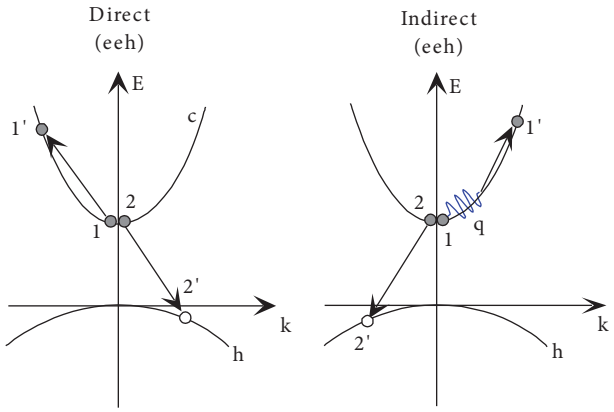

Figure 1. Direct (left) and indirect (right) *eeh* type processes.

Heretofore, it appears that the efficiency degradation at high optical excitation levels is more readily observed in only the high quality LEDs structures [21,22]. The debate naturally centers around whether this is due the Auger process and, if so, it would require a careful examination, the least of which would be the confirmation of the power 3 dependence of generated electrons. The issue to be considered is at what injection levels this degradation is observed, and further whether this is relevant in comparison to the injection levels prevalent in commercial LEDs, which operate at current densities below 10 A cm^{-2}. If one were to assume that Auger recombination is the dominant factor then the InGaN based lasers, which operate at several kA cm^{-2}, would be very adversely affected by this process. One would then surmise that the availability of high power InGaN CW lasers would raise questions about the dominance, not necessarily the presence, of the Auger process. However, Auger recombination at high injection currents has initially been, and continues to be, proposed for the efficiency degradation [5–7,23].

The Auger recombination coefficient deduced from a fit of the rate equation to the experimental photoluminescence (PL) data in an earlier effort is 1.4–2.0 $\times$ 10^{-30} cm^6/s for quasi-bulk InGaN layers [5]; however, the values extracted from EL measurements of LED structures vary by several orders of magnitude among different reports, 10^{-32}–10^{-24} cm^6 s^{-1}, the latter group of figures being some 3 orders of magnitude or more higher than the other reported values [1,5,6,24–27]. From the analysis of the below-threshold efficiency of blue laser diodes (LDs), Ryu et al. [28] have found the Auger recombination coefficient at high carrier densities to be $\sim$3 $\times$ 10^{-31} cm^6/s. Note that the direct Auger recombination coefficient decreases exponentially with the bandgap energy if the process involves transitions across the gap [20], which is supported by a fully microscopic many body model [20]. Calculated Auger recombination coefficients for the direct band-to-band transitions in InGaN are below $\sim 10^{-32}$ cm^6/s [29], and thus should easily be ruled out, at least one would think, for the observed reduction in efficiency at high injection levels. The C coefficient associated with the indirect Auger process is approximately an order of magnitude larger ($\sim 10^{-31}$ cm^6/s for phonon assisted [29] and $\sim 3 \times 10^{-32}$ cm^6/s for the alloy disorder assisted process [30] or even smaller in some other estimates, e.g. similar calculations performed within a Green function technique predicted somewhat lower values and a stronger dependence on the energy gap [9]). Both calculations of the indirect Auger, Refs. [9] and [30], neglect quantization effects, which may not be well taken for narrow active regions (wells). A resonant interband (2.5 eV) Auger process yielding $C = 2 \times 10^{-30}$ cm^6/s was proposed by Delaney et al. [6], based on the first-principle density-functional theory. However, the probability of this interband Auger recombination process, due to resonance between the lowest

and the immediately upper conduction bands, should plummet rapidly with changing wavelength on either side of 2.5 eV. However, experimentally, the efficiency degradation gets worse with increasing wavelength. Later investigations found the effect to be far weaker than originally proposed [29]. It is now accepted that direct Auger recombination is negligible in bulk InGaN (at least for In molar fractions corresponding to blue and green emission) as well as in comparable wide bandgap material systems [31].

The experimentally determined Auger coefficient, which simply relies on 3rd order polynomial fitting of the efficiency vs. injection current/carrier density, may be skewed. This is because of the important effects such as carrier overflow and the very questionable assumption of injection independent not just C but also 3 A, B, and C coefficients. Not all, but representative data of the C coefficient for InGaN and other compounds are shown in Figure 2. If the values of C coefficient extracted from the aforementioned fits of EQE of LEDs vs. injection current density were considered reliable, the III-nitrides would represent a very peculiar case among all the known compound semiconductors. It should also be noted that the C coefficients determined as such encompass a wide range and could probably be overestimated due to varying degrees of current crowding, which is not necessarily taken into consideration in these estimations.

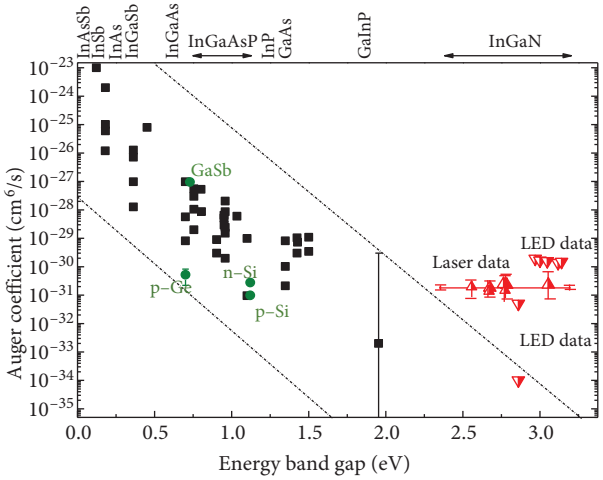

Figure 2. Reported Auger recombination coefficient vs. bandgap for various semiconductors including conventional IIIVs and InGaN (deduced from LEDs and lasers, the latter being more reliable). The dashed lines show the corridor for the Auger coefficients in all the known semiconductors except for III-nitrides. Some data points are courtesy of Dr J Piprek and Prof A Hangleiter.

On the calculation front, Auger coefficients in InGaN/GaN QWs were estimated by multiplying ab initio bulk indirect coefficients and overlap integrals between electron and hole subbands [30]. This simplified approach, adopted also by some experimental groups [32,33], is not in harmony with standard microscopic theories of Auger recombination in QWs [34–39], which rely on multiband $\mathbf{k}\cdot\mathbf{p}$ models within the envelope-function approximation (EFA). These $\mathbf{k}\cdot\mathbf{p}$ EFA theories, developed for conventional III–V compound semiconductors, predicted a significant enhancement of Auger rates due to the lack of momentum conservation along the confining direction. Although successful for zincblende quantum systems, the application of EFA theories to GaN-based QWs led to discordant results [20,40,41]. Vaxenburg et al. [40,41] argued that sharp interfaces of the wells lead to high momentum contributions to the wavefunctions, resulting in Auger coefficients high enough to account for the efficiency degradation. The dependence on the confinement potential was also investigated in Ref. [20] by comparing results for quantum wells with step-like interfaces to those in quantum wells with Gaussian broad-

ened potentials. However, no strong influence of the details of the potential was found. These discrepancies may, at least in part, be explained by possible inconsistencies and intrinsic limitations of the underlying $\mathbf{k}\cdot\mathbf{p}$ model of the sub-band structure. For example, at present there is no consensus over which $\mathbf{k}\cdot\mathbf{p}$ parameters should be used for III-nitrides and the effect of different parameterization (e.g., crystal-field and spin-orbit splitting). Moreover, the description of localized states in narrow QWs may involve bulk states with large wavevector components, well beyond the validity of the underlying perturbative $\mathbf{k}\cdot\mathbf{p}$ model. An additional issue arises in the study of GaN-based QWs, as Auger transitions in wide gap materials involve both confined states near the band edges and excited states that lie far above the gap. This necessitates a unified full-Brillouin-zone (FBZ) treatment of both localized and extended states. FBZ calculations indicate that direct Auger transitions in confined InGaN/GaN structures are (i) enhanced by the lack of momentum conservation along the confining direction, (ii) have a strong dependence on the well thickness with peak values comparable with those of bulk phonon-assisted processes, and (iii) increase, although not dramatically, with the polarization fields as a result of the increased spectral content of the confining potential [42]. To cap this discussion, despite the need for improvement, the existing theoretical approaches as they are implemented suggest the direct Auger coefficient is sufficiently large for us to most likely rule out this process from the discussion. This leaves the indirect Auger process to reckon with if the Auger process is deemed applicable. Clearly, refinement on both the experimental and theoretical fronts is needed to be more definitive.

3. Genesis of efficiency loss in InGaN-based LEDs at high injection

The physical origin of the electroluminescent (EL) efficiency loss at high injection levels in InGaN-based LEDs is not completely understood owing in part to the complexity of modern LED designs. Despite remarkable progress from the performance point of view, the efficiency degradation problem in high injection devices continues to receive considerable attention with many controversial reports in the literature. Whether Auger recombination is something to be reckoned with depends on the value of the inherent C coefficient, not necessarily that deduced from a polynomial fit to the efficiency vs. current curve, which is very dispersive to say the least both in terms of calculations and experiments.

To illustrate the effect of the recombination coefficients on efficiency, which is instructive, Figure 3 compares the experimental dependences of EQE on the injected carrier density with the simulated internal quantum efficiency (IQE) of blue LEDs using the nonradiative Auger coefficient [30] The IQE value η_{IQE} as a function of injection current density has been calculated through the relationship (any possible carrier overflow does not enter into the internal quantum efficiency term):

$$\eta_{IQE} = \frac{Bn^2}{G} = \frac{Bn^2}{An + Bn^2 + Cn^3}. \tag{11}$$

The values typical for InGaN LEDs [66] were used for A, B, and C coefficients in Figure 3. Assuming no carrier leakage, the injection current densities have been calculated from the carrier densities in the active region using the rate equation, Eq. (2) under steady-state conditions:

$$-\frac{dn}{dt} = An + Bn^2 + Cn^3 - \frac{J}{qd} = 0 \tag{12}$$

where d is the thickness of the active layer. Here no carrier overflow is assumed and, further, the injected carrier density is assumed to vary linearly with thickness, which is a good approximation for very narrow active region

thicknesses. In other words, J/d replaces the ∇J term in Eq. (2). As seen in Figure 3, the injection carrier densities at which the blue-LED efficiency reduces appreciably due to the indirect Auger process [30] are of the order of hundreds of A/cm^2 (see curves 1 and 2). These current densities are characteristic for LDs rather than for LEDs. The efficiency degradation is observed in extreme cases at current densities even below $\sim$5 A/cm^2 in multi-quantum well (MQW) LEDs [7].

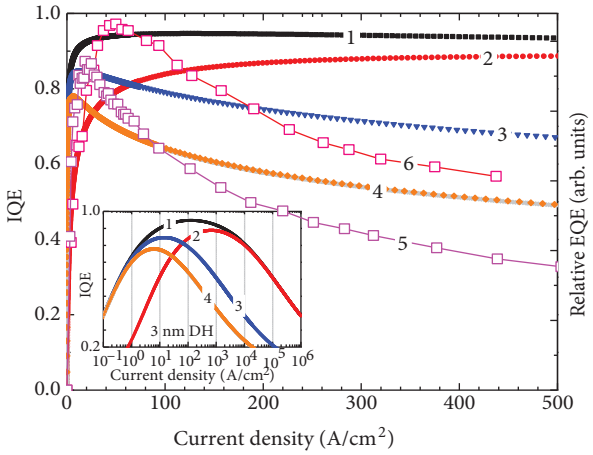

Figure 3. IQE as function of injection current density calculated for blue LEDs with 3-nm wide active region using $C = 2 \times 10^{-31}$ cm^6/s (Auger coefficient reported in Ref. [30]), $B = 5 \times 10^{-11}$ cm^3/s, and nonradiative recombination coefficient A equal to 1×10^7 s^{-1} (curve 1) and 5×10^7 s^{-1} (curve 2). Relative EQEs measured for blue LEDs with 3 nm (curve 5) and 6 nm (curve 6) wide active regions as well as IQE calculated for C equal to 2×10^{-30} cm^6/s (curve 3) and 5×10^{-30} cm^6/s (curve 4) are shown for comparison. The inset shows the calculated IQE within a wider range of current densities in semilogarithmic scale. IQE values for 2 different sets of (A, B, C) coefficients of (4.7×10^6 s^{-1}, 1.1×10^{-11} cm^3/s, 5.2×10^{-31} cm^6/s) and (2.2×10^7 s^{-1}, 2.4×10^{-10} cm^3/s, 5.3×10^{-29} cm^6/s) are indistinguishable from those of curve 4.

The plots shown in Figure 3 illustrate that Auger recombination coefficients of the order of 10^{-30} cm^6/s or larger are required in order to account for the loss of efficiency observed experimentally in LED structures across a wide wavelength range, from UV to green [19]. However, such a large Auger recombination coefficient has so far not been predicted by calculations except for the indirect and resonant processes at 2.5 eV [6]. Unless the indirect Auger process is in effect, one would surmise that the carrier loss to nonradiative recombination due to the Auger effect is unlikely to be the major contributor to the observed efficiency degradation. It should, however, be noted that different sets of A, B, C coefficients can reproduce the same IQE dependence on injection current for a given range of current densities, indicating that the coefficients determined from fits to experimental EQE curves may not be physically meaningful unless at least one of the coefficients is known. Just to demonstrate the point, IQE values corresponding to 2 different sets of (A, B, C) coefficients (4.7×10^6 s^{-1}, 1.1×10^{-11} cm^3/s, 5.2×10^{-31} cm^6/s and 2.2×10^7 s^{-1}, 2.4×10^{-10} cm^3/s, 5.3×10^{-29} cm^6/s) are indistinguishable from those of curve 4 in Figure 3 despite the 2 orders of magnitude difference in the C coefficient used.

3.1. Direct observation of Auger electrons

On the heels of the above mentioned arguments, a report emerged that pegs the efficiency degradation in full to the Auger processes through measurement of the electron energy spectrum under bias in a vacuum electron emission spectroscopy realm [8]. In this scenario, the electrons kicked up high in the conduction band during the Auger process traverse through the remaining active layer, any EBL, and the p-layer before being emitted into vacuum, assuaged by Cs vacuum-coated LED surface, and their kinetic energy spectrum is measured. In the process, the L satellite band edge is also determined as some of the electrons finish their journey to the surface while still in the L-band, which was used as the basis for the argument that electrons scatter from high up in the Γ-band to the L-band, with a characteristic scattering time shorter than 180 fs [43]. Through an accounting scheme, electrons collected in the energy analyzer together with reduction in efficiency by the nonradiative electrons were correlated. The total yield of Auger electrons was estimated to be in the order of 10^{-6}. The efficiency degradation was solely attributed to the Auger process.

It might appear that this is an open and shut case and the perplexing nature of efficiency loss is unambiguously explained. While the emission of electrons into vacuum in the experiments must be taken as being very credible, some questions arise nonetheless. For the purpose of calibrating our frame of mind with the help of Figure 4, the bandgap of InGaN emitting in blue is about 2.8 eV, which means that, assuming 70% conduction band edge discontinuity, electrons kicked up by the Auger process would be 2.38 eV above the Γ conduction band edge of GaN and 1.48 eV above the bottom of the L-band. From vacuum photoemission experiments [44,45], the Γ-L band separation is estimated as $\sim 0.90 \pm 0.08$ eV, which is significantly lower than those determined from spectroscopic ellipsometry measurements [46,47] (see below for further details) and ab initio calculations [48].

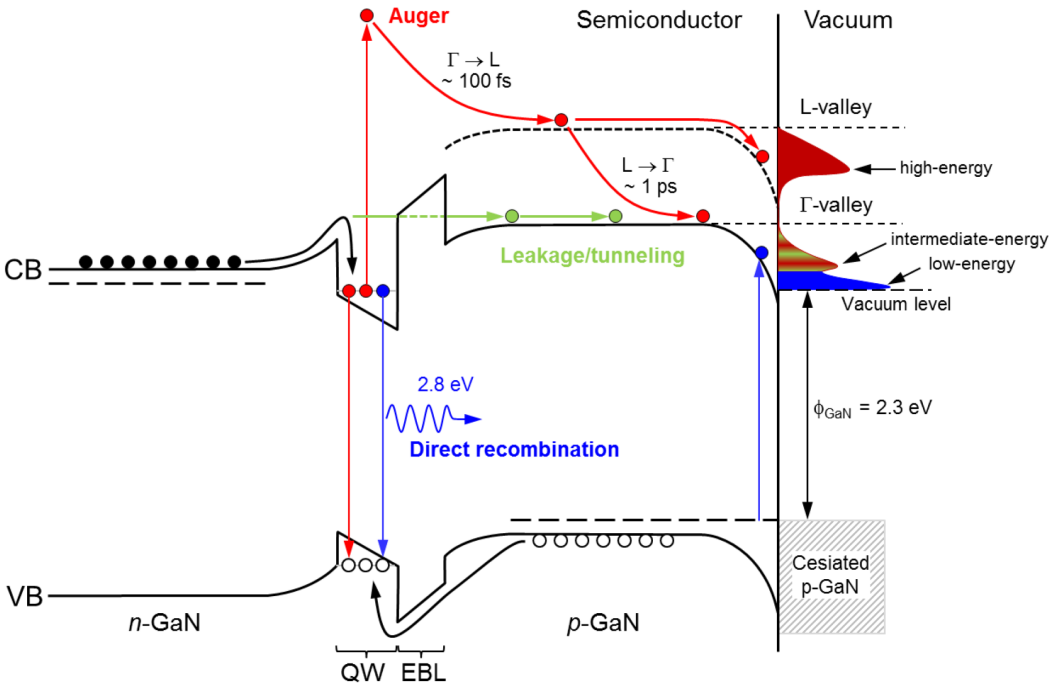

Figure 4. Carrier transport mechanisms in the vacuum electron emission experiments. (Patterned after Refs. [8] and [44]).

While travelling toward the surface, scattering down to the bottom of the Γ-band would require some 26 LO phonon emitting processes. During this cooling, the electrons are likely to transfer to the L-valley as the L-valley has higher density of states and the $\Gamma \rightarrow$ L scattering time ($<$ 180 fs) is shorter than the cooling time considering that the LO phonon emission time is ∼20 fs. Reabsorption of hot phonons slows down the electron energy relaxation because the number of emission events increases. Auger electrons that scatter into the L-band would cool to the bottom of the L-band before they can be transferred back to the Γ-band as the $L \rightarrow \Gamma$ scattering time is $\sim$ 1 ps and the total depopulation time of the L-band is $\sim$ 20 ps [43]. Ironically, the larger the bandgap, the hotter the electrons and more scattering events can be tolerated before possible recombination in the p-layer. The electrons thermalized in the Γ-band are assumed to recombine nonradiatively in p-GaN without being able to reach the surface and be emitted into vacuum, as the diffusion length (10–30 nm used in Ref. [44], but 100 nm in Ref. [8]) is smaller than the p-GaN thickness (200 nm). The low energy peak observed in the energy distribution curves (Figure 4) is, therefore, attributed to photoexcitation in the 10-nm-wide band bending region near the surface by the 2.8 eV light emitted by the LED due to impurity band or Franz–Keldysh transitions, which results in emission of electrons within the Γ-band.

This premise was further confirmed by photoexcitation measurements on a separate sample with optical excitation mimicking the LED emission [44]. If the electrons travelling toward the surface while in the L-band scatter back to the Γ-band within a diffusion length from the surface or in the band bending region, then they can be emitted into vacuum from the surface and registered as "intermediate" energy electrons (0.3–0.4 eV above the low energy peak) in the energy distribution curves. Based on the relatively long (20 ps) total depopulation time for the L-valley ($L \rightarrow \Gamma$ scattering time $\sim$ 1 ps) [43] it is assumed that only the electrons cooled to the bottom of the L-band can reach the surface and experience additional cooling in the band bending region before they are emitted into vacuum, resulting in the high energy peak ($\sim$ 1.5 eV above the low energy peak) in the energy dispersion curves. This high energy peak associated with Auger electrons emerges at a current density of 0.5 A/cm^2, which corresponds to an electron density of $\sim 3 \times 10^{17}$ cm^{-3} deduced from the ABC model using $A = 1 \times 10^6$ s^{-1}, $B = 2 \times 10^{-11}$ cm^3 s^{-1} , and $C = 1 \times 10^{-29}$ cm^6 s^{-1} (76 % peak IQE). For the same injection current density, absence of the high-energy peak in GaN p-n junction diodes, where the resulting carrier density is much lower compared to that in MQW LEDs, suggests that the high energy electrons are most probably of Auger origin.

The notion of L electrons traversing the remaining length of the active region, the EBL and the p-layer, which could amount to some 250 nm, is not consistent at the moment with the current predictions as the estimated deformation potential scattering rates might be as high as 10^{14} s^{-1} (deformation potential scattering rate is proportional to the phonon wave vector, and, therefore, is mainly an intervalley process connecting the satellite valleys with the Γ-valley; polar optical LO scattering is the most probable process for small phonon wavevectors, and, therefore, provides an efficient intravalley relaxation channel). It has been suggested that the relaxation could be slower if hot phonons are considered (LO phonon scattering times of 20 fs to 200 fs are considered in Ref. [44] and 9 fs in Ref. [8]). However, it should be noted that hot-phonon effects would be prominent under near-equilibrium conditions, where most electrons may not have sufficient energy to emit a phonon, thus favoring phonon re-absorption, which in a sense would slow down the relaxation process. As the Auger carriers have high energy far above the LO phonon threshold this situation is unlikely for the experimental scenario described. For a scattering rate of the order of about 10^{14} s^{-1} in the Γ-band, the transit distance might be 40–80 nm. One point that should be made is that when the p-layer thickness is increased to 500 nm, no vacuum emission of high energy electrons is observed, which means that they undergo recombination in

the p-layer before reaching the surface. Moreover, LEDs with 100-nm-thick p-GaN and no EBL were found to exhibit no significant change in the low-energy peak behavior compared to the LED with 200 nm p-GaN and an EBL, indicating still no contribution from Auger electrons quickly thermalized in the Γ-band even for this much thinner p-GaN and increased injection of cold electrons due to the absence of an EBL [44]. Clearly, the discrepancy between the experiments and theory requires more refinement.

Delving more into the vacuum emission realm with an eye of a critic, available full-band Monte Carlo simulations, taking into consideration all the relevant scattering processes, predict that Auger electrons emitted in the active region, below EBL, would thermalize in the Γ-valley to the bottom of the conduction band minimum in less than half the p-cap thickness typically used (200 nm) before reaching the band bending region (BBR) [49,50]. These calculations are not consistent with experimental observations that Auger electrons are collected from the satellite L-valley, which is predicated on the notion that the electrons do not undergo significant cooling towards Γ before reaching the BBR. As discussed above, it was suggested in Ref. [8] that high-energy Auger electrons would quickly thermalize (due to the very heavy effective mass of electrons in the L-band), in a long-lived L-valley (meaning scattering rate to the Γ is very small) and would cross the 200-nm-thick highly doped GaN p-cap (plus a 40-nm-thick electron blocking layer) with a transit time estimated at 1 ps, corresponding to a velocity of about 2×10^7 cm/s (Ref. [8]) (a collision time of 20 fs with LO phonons is assumed to lead to 24 nm mean free path for 1 eV electrons [44]). However, this velocity implies ballistic-like transport, which seems inconsistent with the premise that *thermalized* electrons populate the L satellite valley. We should keep in mind that diffusion is the only viable transport mechanism for thermalized electrons in a region where the electric field is negligible and the effective mass is large. In order to have a sizable fraction of carriers that traverse a distance of 240 nm in the L satellite valley, one would have to assume a scattering time from L to Γ in excess of 100 ps (under the assumption that the electrons thermalize in the L-valley, the transport would therefore be diffusive and a highly optimistic mobility is about 200 $\mathrm{cm}^2\ \mathrm{V}^{-1}\ \mathrm{s}^{-1}$), which is longer than the total L-valley depopulation time of 20 ps used. At the moment this is inconsistent with the available theory dealing with the computation of the intervalley deformation potential scattering rates [51,52].

Continuing on, at the lowest injection current (4 mA), the higher-energy peak was found at 1.5 eV above the vacuum level (see Fig. 2 of Ref. [8]), i.e. just 0.5 eV above the bulk Γ conduction band edge. As the energy difference between the intermediate peak in Figure 4 (originating from the electrons scattered back to the Γ-band near the surface region) and the high energy peak (resulting from the Auger electrons) remains nearly constant at $\sim$ 1 eV, the electrons would be expected to go through additional cooling in the band bending region. However, the width of the band bending region is only 10 nm [45], which should allow mainly quasi-ballistic transport.

All modern density functional theory (DFT) calculations of electronic structures that are available at the time of writing place the satellite valleys in GaN at energies more than 2 eV above the conduction band edge [53,54], much larger than the observed higher-energy peak. It should be noted that despite these relatively large satellite band separations emanating from band structure calculations, except for a very few reports such as the 1.49 eV value in Ref. [55], some experimental works report lower values: 1.1 eV [43], 1.2. eV [56], and 1.34 eV [57], somewhat consistent with the observations from photoemission spectroscopy [45]. However, direct experimental measurements of the critical points (van Hove singularities) in wurtzite GaN by spectroscopic ellipsometry provide very reliable values near 7 eV for the second critical point (E_1) after the 3.42 eV Γ-band (E_0) as shown in Figures 5a and 5b [46]. The critical points observed up to 10 eV are indicated on

the calculated band structure of GaN in Figure 5c [58]. Note than $E_1(C)$ transition is forbidden for E//c polarization. Assuming an even split of the excess energy between the conduction and valence bands, the lower limit of the Γ–L band separation in the conduction band can be obtained as 1.8 eV, higher than that measured in vacuum photoemission experiments [45]. Indeed, a more reliable number deduced from ellipsometric measurements and available band structure is near 2.6 eV [59].

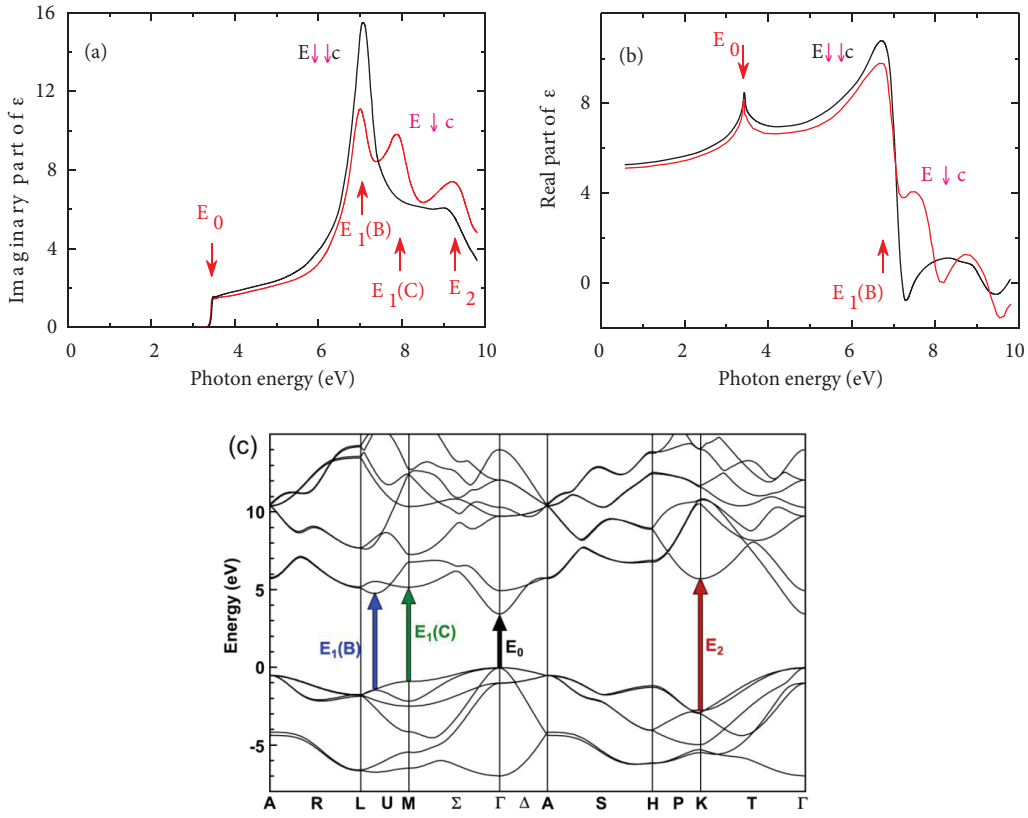

Figure 5. (a) Imaginary and (b) real parts of the dielectric function of wurtzite a-plane GaN measured by spectroscopic ellipsometry for polarization parallel and perpendicular to the c-axis (courtesy of Prof R Goldhahn and Dr M Feneberg). (c) Calculated band structure (courtesy of D Fritsch et al. [58]) along with the measured critical point energies indicated.

Allowing our wonderment to go unbounded, other thought-provoking issues come to mind. For example, because hot electrons are not subject to inelastic scattering mechanisms other than the intrinsic processes involving a variety of phonon interactions/deformation potential, one could argue that the layer quality would not be an overriding concern. However, this is not consistent with observations as the above discussed experiments are apparently better conducted in high quality commercial LEDs. Another similar thought-provoking issue is that the devices utilizing wide bandgap materials would be more conducive to successful hot electron transit to the surface as it would take many scattering events for electron thermalization and subsequent recombination. Considering that the direct Auger process is less likely in wider gap materials and yet the Auger process is assumed to be taking place to an extent as to account solely for the efficiency loss, one must then evoke the notion that the Auger process that is taking place must then be the indirect Auger variety, which would be more likely in relatively low quality material if alloy and compositional fluctuations are involved. As

alluded to above, missing also from the above arguments is the hot electron dynamics with required specificity. More incisive and quantitative arguments will need to wait until such time as reliable inter- and intravalley scattering rates as well as refined upper conduction band energies become available.

3.2. Optical excitation experiments and Auger process

Returning to more conventional experiments, there are also other observations, which are not consistent across the board with the Auger recombination premise. For example, consider below the barrier resonant photoluminescence (PL) experiments, in which the photons are absorbed only in the InGaN active region with ensuing photo excitation of equal numbers of electrons and holes followed by their thermalization and either radiative or nonradiative recombination only in the same region. In the resonant PL experiments, no Auger kicked hot electrons exist and the internal quantum efficiency (IQE) degradation has not been noted at photo carrier generation rates comparable to, if not beyond, the electrical injection levels where the EL efficiency shows degradation [11,13]. If the Auger process, particularly the indirect one mediated by phonons or alloy scattering, came into the picture at the injection levels of the order of hundreds of A/cm^2, this should be observable in resonant PL experiments at high excitation densities. The IQE reduction has been observed by Mickevicius et al. [60,61] in GaN and AlGaN at extremely high excitation powers, of the order of MW/cm^2, close to the onset of stimulated emission and much higher than that experienced in LEDs.

Contradicting the above mentioned observations, Binder et al. [62] investigated 2 color structures wherein when the longer wavelength layer (green) is resonantly excited, the shorter wavelength (UV) region emits light, which was attributed to hot electrons created by the Auger process in the longer wavelength layer (green) traversing to the shorter wavelength one (UV) followed by radiative recombination. This report, however, is void of quantum well (QW) thicknesses and excitation power density levels used. Moreover, Hader et al. [63], using a fully microscopic model to emulate this particular experiment, argue that a resonant laser tuned to create carriers only in the green region does also create carriers in the UV region even in the absence of any Auger process. The reason provided is that the polarization excited by the spectrally narrow optical pulse dephases in a few tens of femtoseconds due to electron–electron and electron–phonon scattering. In this scenario, the free carriers are generated through coupling between the optical pulse and the associated material polarization, causing the total spectral width of the excitation to be dominated by dephasing time of the polarization, not by that of the optical pulse. The resulting spectral width is argued to be sufficiently wide to excite the UV QW as well. Due to the very small coupling between the states in the green region and those of the UV region, the carriers generated in the UV region do not relax to states in the green region, which paves the way for UV emission. In our very own experiments dealing with 2 color systems, the resonant excitation of the blue QW region using a frequency doubled Ti:Sapphire laser of $\sim$ 100 fs pulsewidth and 80 MHz repetition rate did not result in any detectable emission from the UV QWs (400 nm) up to the maximum laser excitation density that can be applied in our lab, which corresponds to a carrier density of 10^{19} cm^{-3}, much larger than the injection densities employed in LEDs, as can be seen in Figure 6. It should also be noted that this carrier density is estimated using the steady-state approximation, which certainly is not fully valid for the pulsed excitation conditions used, and, therefore, represents an average value and only a lower limit of the instant carrier density within the active region.

When the 2-color LED mentioned above was excited using a 1 kHz repetition rate 130 fs pulsewidth optical parametric amplifier (425 nm wavelength) providing much higher photon fluences allowing clear observation of 2-photon absorption related emission from all layers, still no evidence of Auger recombination related transfer

of hot electrons from the blue QW to the UV QW was observed. Figure 7a shows the PL intensities for the UV and blue QWs as well as the underlying GaN layers as a function of the excitation density. Under the excitation conditions used the PL intensities from the UV and blue QWs are proportional to Bn_{UV}^2 and Bn_{blue}^2, where n_{UV} and n_{blue} are the electron densities in the UV and blue QWs, respectively. If Auger recombination were effective in the blue QWs, their generation rate (Cn_{blue}^3) would be equal to the generation rate in the UV QWs (Bn_{UV}^2 under steady-state) following hot electron transport from the blue QWs under the assumption that Auger recombination in the UV QWs and the SRH recombination overall at 15 K are negligible. This would then imply that the intensity from the UV QWs should exhibit cubic dependence on the square root of the intensity from the blue QWs. However, the observed dependence above the threshold for the UV QW emission is to the 6th power as shown in Figure 7b.

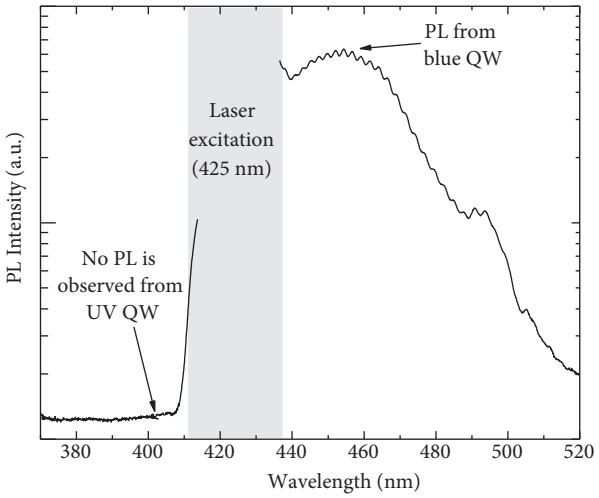

Figure 6. With 425 nm excitation at 15 K, only the PL peak from low energy blue QW (460 nm) can be observed at an excitation density corresponding to 10^{19} cm^{-3} photo-generated carrier concentration. Note the lack of emission from the larger bandgap UV QW (400 nm). The spectral range near the excitation laser line is blocked.

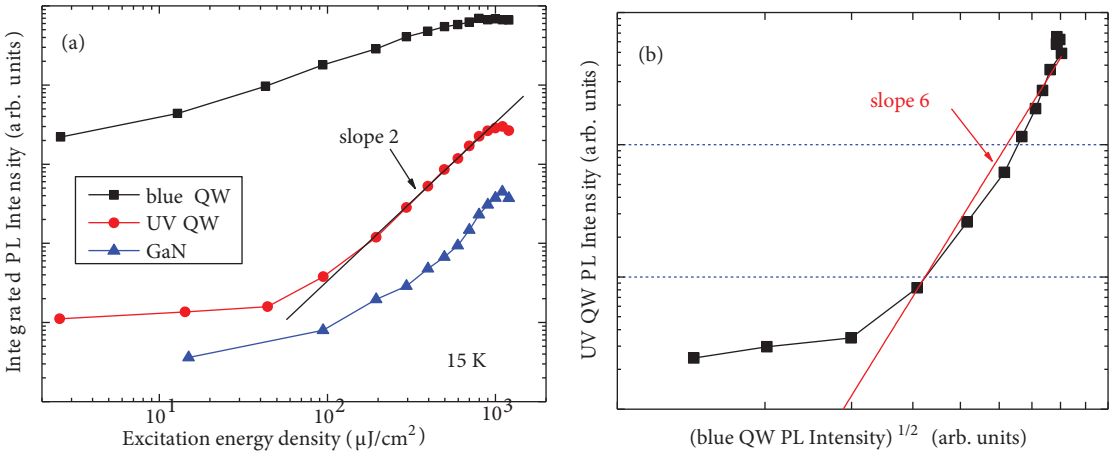

Figure 7. (a) Integrated PL intensities for the UV and blue QWs and the GaN layer in the 2-color LED with 425 nm excitation at 15 K. (b) PL intensity from the UV QWs versus the square root of the PL intensity from the blue QWs, which is proportional to the electron density in the blue QWs, n_{blue}.

The observed quadratic dependence of the UV QW PL on excitation density (Figure 7a) suggests that the UV emission is due to generation of carriers in the UV QWs by 2-photon absorption. The same quadratic dependence is observed for the PL from the underlying GaN layer. It can, therefore, be concluded that the Auger recombination is not effective at carrier densities that correspond to the threshold for UV emission, beyond which significant 2-photon absorption occurs. The average carrier density estimated for the threshold excitation density value of 100 μJ/cm^2 is 2 $\times$ 10^{19} cm^{-3}, which, as indicated above, represents only a lower limit due to the femtosecond pulsed excitation used.

Although the Auger process is likely to manifest itself at so high excitation power densities, heating effects are enormous to be excluded. As shown in Figure 8, for a MQW LED sample composed of six 1.5-nm-thick QWs, the PL efficiency increases with excitation density (Figure 8a) and reaches its peak value at a corresponding average photogenerated carrier density of 10^{18} cm^{-3} at room temperature (Figure 8b), the density being dependent on the radiative recombination coefficient assumed. As expressed above, the maximum photogenerated carrier density is much higher due to the femtosecond pulsed excitation used. The IQE, defined

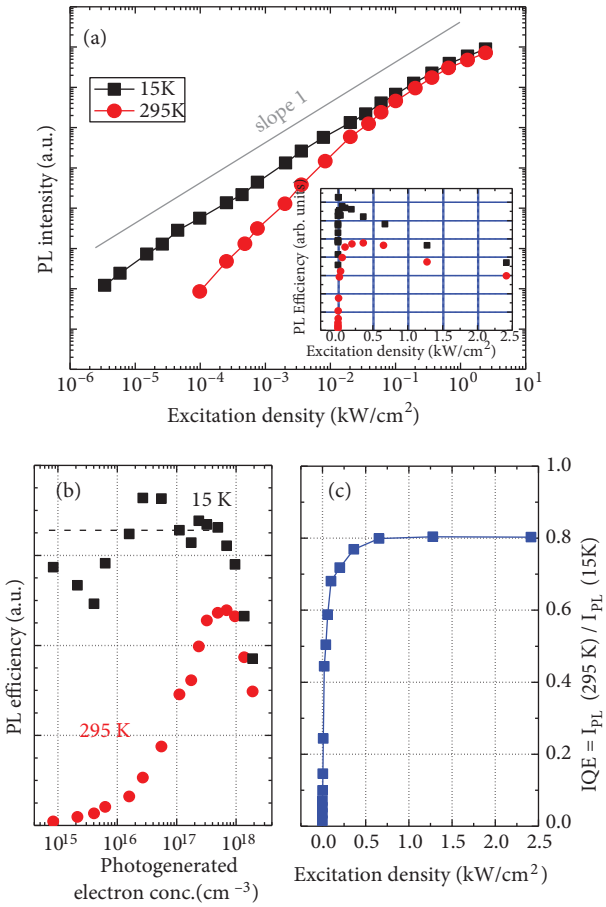

Figure 8. (a) Integrated PL intensity as a function of excitation density for a MQW LED samples with six 1.5 nm $In_{0.15}GaN$ QWs at 15 K and 295 K. The inset shows the PL efficiency at both temperatures. (b) PL efficiencies at 295 K and 15 K as a function of the carrier density estimated using $A = 10^7$ s^{-1}, $B = 5 \times 10^{-11}$ cm^3/s, and $C = 2 \times 10^{-31}$ cm^6/s. Note that temperature dependence of these coefficients is not taken into consideration. (c) IQE calculated from the ratio of PL intensity at 295 K to that at 15 K.

as the ratio of PL intensity at room temperature to that at 15 K, does not indicate any drop from the 80% value with increased excitation as shown in Figure 8c, which is problematic unless the quantum efficiency is 1 at low temperature. Therefore, it is important to note that this commonly used approach for IQE evaluation may not be reliable since low-temperature PL efficiency might be decreasing with increasing excitation density, as observed for this particular LED structure (Figure 8). These observations suggest that the EL efficiency degradation in InGaN LEDs at injection current densities of practical interest for general lighting is primarily of electrical nature and that it is very likely to be related to carrier injection, transport, and leakage processes as well as relatively low hole concentration on the p side of the junction.

The above discussion allows the narrative for the electron overflow as possibly being the primary cause for reduction of EQE as the injection is increased unless the design is optimized, while other effects being aggravating factors to varying degrees. It has been observed that a substantial EL efficiency reduction (by 4–5 times) occurs when an electron blocking layer (EBL) is not employed, regardless of whether polar or nonpolar orientations of GaN are used [64]. In InGaN LEDs, while not being the entire reason at this juncture, relatively low hole injection (due to relatively low hole doping of p-GaN) and/or poor hole transport inside the active region (due to large hole effective mass if quantum wells constitute the active region) could exacerbate the electron overflow, as electrons need accompanying holes in the active region for recombination [13,65]. Theoretical calculations also indicate that electron density in equilibrium with the lattice even well above the room temperature would not have a sufficient Boltzmann tail to surpass the barrier present for notable electron spillover [66]. This further narrows the discussion in that the nonequilibrium processes must be invoked to account for electron overflow. Evidence for ballistic transport and the associated electron leakage has been obtained from the temperature dependent characteristics of InGaN LEDs and LDs [67–69]; however, ballistic electron transport has so far been included in the analysis of electronic devices only [1,70]. Özgür et al. [66] have demonstrated that the inclusion of the electron overflow term into the rate equation can indeed represent the efficiency loss at high injection observed experimentally in LEDs. Lin et al. [71] have confirmed these results, salient aspects of which are discussed below.

4. Electron overflow: hot electron model

The electron overflow in semiconductor heterostructures can originate from 2 processes: (i) thermionic emission of equilibrium electrons from the bottom of the conduction band in the active region over the barrier into the p-layer; (ii) ballistic and quasi-ballistic transport of the injected electrons. However, as we demonstrate immediately below, the large band discontinuities make sizable contribution from the former process to the electron overflow unrealistic in the InGaN system [72]. The hot-electron ballistic and the quasi-ballistic transport in the InGaN LEDs have been considered in detail in our earlier papers [72–74]. Following a brief discussion of the thermionic emission, we will discuss the impact of hot electrons on the electron overflow.

4.1. Electron overflow due to thermionic emission

By using Silvaco Atlas software, we simulated carrier overflow in the p-GaN/$In_{0.20}Ga_{0.80}N$/n-GaN LED without an EBL while taking into account thermionic emission of equilibrium electrons and tunneling within the Wentzel–Kramers–Brillouin approximation [72]. The commonly accepted Shockley–Read–Hall (SRH) recombination coefficient of 1×10^{7} s^{-1} and spontaneous radiative recombination coefficient of 1×10^{-11} cm^{3} s^{-1} were used for the $In_{0.20}Ga_{0.80}N$ active layer. The Auger recombination coefficient was assumed to be 1×10^{-30} cm^{6} s^{-1}. For p-GaN, the SRH coefficient of 1×10^{10} s^{-1} (corresponding to a lifetime of 100 ps) was used.

The conduction band offset $\Delta E_c = 0.5$eV. was taken to be 70% of the total band gap discontinuity between InGaN and p-GaN. The simulations showed that even at an uncharacteristically high junction temperature of 1000 K and at an unreasonably high current density of 1×10^4 A cm^{-2} the thermionic emission driven overflow electron current into the p-GaN region due to electrons in thermal equilibrium with the lattice is only $\sim$11% of the total current density. For junction temperatures of 700 K and 500 K and the same current density of 1×10^4 A cm^{-2}, the corresponding overflow currents are $\sim$1% and $\sim$0%, respectively [66,72]. Considering the large discrepancy for the Auger coefficient [5,6,7,26], the calculated electron overflow values would be 0%, 3%, and 36% for junction temperatures of 500 K, 700 K, and 1000 K, respectively, if an Auger coefficient of 1×10^{-34} cm^6 s^{-1} is assumed instead.

The thermionic emission being inconsequential suggests that we must turn our attention to nonequilibrium electrons in the active region. The injected hot electrons can travel across the active layer by ballistic or quasi-ballistic transport, unless blocked by EBL, and recombine in the p-GaN region instead of the active region and thus not contribute to light emission at the desired wavelength. Below, we discuss our calculations of ballistic and quasi-ballistic transport of electrons through the active region and attempt to explain the data for LEDs with varying barrier height of the EBL and electron injectors and active regions of various designs in this framework.

4.2. Electron overflow due to hot electron transport

The electrons acquire additional kinetic energy equal to the conduction band offset between n-GaN and $In_{0.20}Ga_{0.80}N$ (ΔE_c, $\sim$0.5 eV in this case) upon injection. These hot electrons would either undergo thermalization and lose their excess energy mainly through interaction with LO-phonons [75] or avoid thermalization and leave the InGaN region as depicted in Figure 9.

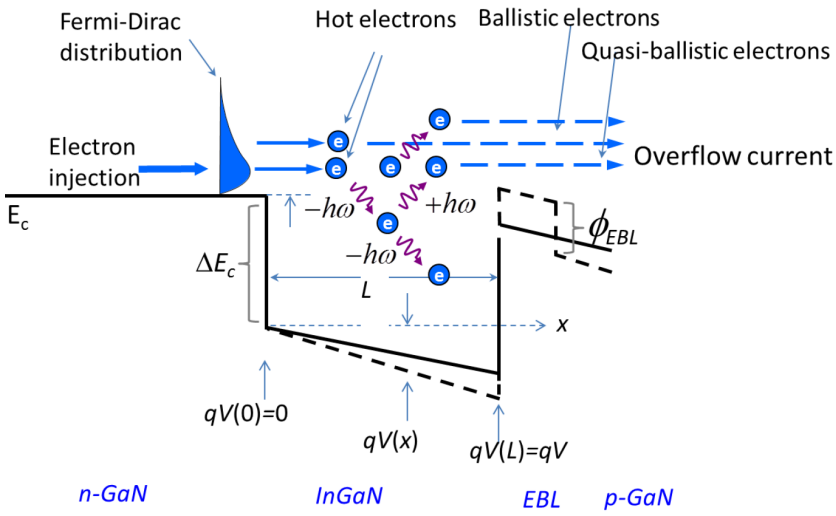

Figure 9. Schematic of electron overflow caused by ballistic and quasi-ballistic electron transport across the InGaN active region. The electrons gain a kinetic energy after being injected into InGaN, which equals $E+\Delta E_c+qV(x)$. These hot electrons will either traverse the active region ballistically and quasi-ballistically, avoid recombination inside InGaN, and contribute to electron overflow current, or be thermalized and captured inside the active region through interactions with LO-phonons. Dashed lines in the band structure represent additional band bending caused by the piezoelectric field due to EBL.

The calculations discussed below take into account the ballistic electrons, representing those that experience no scattering in the active region, and the quasi-ballistic electrons that experience one scattering event (i.e. either LO phonon emission or absorption), and 2 scattering events. The latter case includes 4 combinations of 2 scattering events involving LO phonon emission and absorption. Electrons experiencing multiple energy losing scattering events are eventually thermalized. In the calculations the electrons are categorized according to the scattering events they experience: no scattering, 1 scattering event (one LO phonon emission or one LO phonon absorption), etc. It should be noted, however, that the contribution to the overflow from electrons undergoing 2 or more scattering events is a negligible 1% [72]. Therefore, we consider only 3 cases: (i) no scattering, (ii) 1 phonon emission, and (iii) 1 phonon absorption. In the following consideration, we assume the Fermi–Dirac energy distribution of electrons in the n-GaN layer, i.e. before they are injected into the active region. Moreover, for simplicity we assume that electrons travel only in the direction normal to the heterointerfaces, which would result in insignificant overestimation of the current overflow as the angular distribution of the scattered electrons is narrow after 1 or 2 LO emission events. As a result, the one-dimensional analysis presented here is sufficiently accurate.

4.2.1. Truly ballistic case

As illustrated in Figure 9, at position x inside the InGaN layer of thickness L, the kinetic energy of an electron is $E+\Delta E_c+qV(x)$, where E is the excess energy in the $n-$GaN layer with respect to the conduction band of $n-$GaN, due to e.g. band bending and kinetic/thermal energy, ΔE_c is the conduction band offset between the InGaN and the $n-$GaN, and $V(x)$ is the net potential drop within the active region at position x due to the electric field (including the effect of the built-in potential) with boundary conditions of $V(0)=0$ and $V(L)=V$. Therefore, the electron velocity at position x is $v\left(E+\Delta E_c+qV(x)\right)=\sqrt{2\left(E+\Delta E_c+qV(x)\right)/m_e}$, where m_e is the electron effective mass. Then the total time for the electron to cross the active region is $t=\int_0^L dx/v\left[E+\Delta E_c+qV\left(x\right)\right]$. The probability of the ballistic transport at a given energy is proportional to $\exp\left(-t/\tau_{sc}\right)$, where t is the transit time, and τ_{sc} is the electron–LO-phonon scattering time given by $\tau_{sc}=1/\left(1/\tau_{abs}+1/\tau_{em}\right)$, where τ_{abs} and τ_{em} are the LO-phonon absorption and emission times, respectively [18]. It should be noted that the phonon scattering time is actually dependent on the electron density and energy, but for simplicity we will assume it to be constant in this treatment [72]. The percentage of the overflow electrons injected from the n-GaN is represented by the product of the probability of electrons to have excess energy $E\geq\max\left\{0,\left(\phi_{EBL}-qV\right)\right\}$ above the conduction band in the n-GaN layer and the probability of electrons to transport ballistically across the active region:

$$P_1=\left[\int_{\max\{0,(\phi_{EBL}-qV)\}}^{+\infty}f\left(E\right)N\left(E\right)\exp\left(\int_0^L\frac{-dx/\tau_{sc}}{v\left[E+\Delta E_c+qV\left(x\right)\right]}\right)dE\right]\Bigg/\left(\int_0^{+\infty}f\left(E\right)N\left(E\right)dE\right) \quad (13)$$

where ϕ_{EBL} is the barrier height of EBL (i.e. the conduction band offset between the EBL and the p-GaN, and it vanishes for the LEDs without EBL), $N(E)$ is the conduction-band density of states, and $f(E)$ is the Fermi–Dirac distribution function.

The calculation of electron overflow by Eq. (13) requires the potential distribution $V(x)$ inside the InGaN layer, which can be performed numerically, e.g., by Silvaco Atlas simulation package.

4.2.2. Quasi-ballistic case

As mentioned already, quasi-ballistic electrons undergoing single scattering events, namely one LO phonon emission or one LO phonon absorption, can also substantially contribute to the overflow in addition to fully ballistic electrons. The total fraction of the overflow electrons that experience 1 scattering event, 1 phonon emission, or 1 phonon absorption is given by (Ref. [72])

$$P_2 = \begin{array}{l}\left(\int_{\max\{0,(\phi_{EBL}-qV\pm\hbar\omega_{LO})\}}^{+\infty} f(E)\,N(E)\int_0^L \frac{1}{v(E+\Delta E_c)\tau_{ph}}\exp\left(-\frac{x/v(E+\Delta E_c)}{\tau_{sc}}\right)\right. \\ \left.\times\exp\left[-\frac{(L-x)/v(E+\Delta E_c\mp\hbar\omega_{LO})}{\tau_{sc}}\right]dxdE\right)/\int_0^{+\infty} f(E)\,N(E)\,dE\end{array} \tag{14}$$

where $+\hbar\omega_{LO}$ and $-\hbar\omega_{LO}$ in the lower integration limit correspond to one phonon emission ($\tau_{ph}=\tau_{em}$) and absorption ($\tau_{ph}=\tau_{abs}$) processes, respectively, and $\hbar\omega_{LO}=88$ meV is the LO phonon energy in InGaN. Eq. (13) takes into account energy conservation and the probabilities of finding an electron in the active region (represented by $f(E)\,N(E)\left[\int_0^{+\infty} f(E)\,N(E)\,dE\right]^{-1}$), an electron reaching position x without being scattered (represented by $\exp(-x/v(E+\Delta E_c)\tau_{sc})$), to emit/absorb an LO phonon between x and $x+dx$ (represented by $dx/v(E+\Delta E_c)\tau_{ph}$), and to exit the active region without being scattered between x and L (represented by $\exp[-(L-x)/v(E+\Delta E_c\mp\hbar\omega_{LO})\tau_{sc}]$. The integration over dx and dE accounts for all possible paths and all suitable electrons.

5. Measurement of electron leakage in the photodiode configuration

The electron overflow in forward biased LEDs must be delineated from the recombination (both radiative and nonradiative) component of the current by means of models that are developed and thus somewhat indirect. If the band structure seen by electrons traversing under forward bias is replicated when the diode is under reverse bias and electrons are traversing to the n-side, one can use the photodiode configuration with optical excitation to measure the electron escape from the active region. The portion of the generated electron-hole pairs that participate in radiative recombination can be estimated by luminescence emanating from the junction. The contribution by the nonradiative component can be neglected as the layer quality nowadays is sufficiently good to justify this assumption. In the experiments we undertook, CW 325 nm HeCd excitation had to be used, which is absorbed by the p-layer, and the fraction of photons absorbed in the active region can only be determined if the minority carrier diffusion length is known. Therefore, we first determined the said diffusion length by progressively thinning the p-layer by a known amount and repeating the luminescence experiments. These experiments led to diffusion lengths of 92 $\pm$ 7 nm and 68 $\pm$ 7 nm at 295 K and 15 K, respectively, which are then used in the estimation of the photons that are absorbed in the active region in conjunction with the photodiode experiments. Figure 10 shows the percentile of electron leakage out of the active region vs. the bias for an LED containing a 6-nm-thick $In_{0.15}Ga_{0.85}N$ active layer and a 10-nm-thick $Al_{0.20}Ga_{0.80}N$ EBL. Naturally an increase with bias ensues because of the band bending due to the bias favoring electron escape from the active region. LEDs and photodiodes are dissimilar in that in the former one desires to have all the carriers to recombine in the active region and the recombination current to the only current component. In the latter one desires to extract all the photogenerated carriers out of the absorption region, which means that a well-designed LED would not make a very good photodetector but for the sake of the experiments discussed here, LEDs can be used in the photodiode realm. The photocurrent method can be used to estimate the carrier overflow in LEDs by investigating structures with barriers of different height inserted on both sides of the active region.

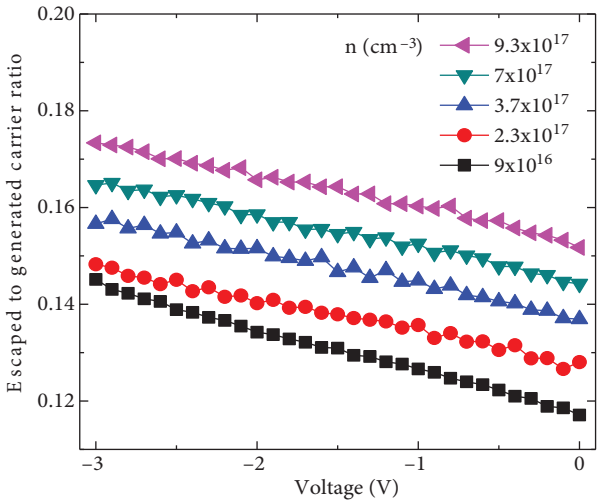

Figure 10. Electron flow percentile out of the active region into the adjacent n-type semiconductor of an InGaN LED used as a photodiode with photogenerated electron density to be the parameter.

6. Electron injector designs to eliminate electron overflow

AlGaN EBL, which is placed between the active region and p-GaN, is usually employed to mitigate the hot electron overflow in InGaN LEDs. However, several shortcomings are associated with the use of EBL in InGaN LEDs. First of all, the EBL impedes hole injection due to the barrier it introduces in the valence band after p-GaN. Using numerical simulations, the reduced IQE in InGaN-based LEDs with EBL due to poor hole transport has been demonstrated by Ryu and Lee [76]. Moreover, the AlGaN EBL is located on top of the InGaN barrier of the active region, and the lattice mismatch between AlGaN and InGaN generates a piezoelectric polarization field in addition to differential spontaneous polarization field. These 2 fields, acting in unison, pull down the conduction band at the AlGaN/GaN interface. As a result, the effective barrier height of the AlGaN EBL is compromised, and the electron overflow is not effectively suppressed [12]. The effective barrier height of the AlGaN EBL can be bolstered with higher Al composition and/or increased thickness at the expense of generation of additional strain-induced defects and larger piezoelectric polarization field. The larger built-in field might lead to band bending and poor carrier confinement and hence could degrade the radiative recombination rate at higher injection levels.

We have demonstrated that the electron overflow and the associated efficiency loss can be effectively reduced by inserting, between the n-GaN/InGaN electron emitter and the InGaN active region, an InGaN electron injector, either with a step-like increased [15,72] or continuously graded indium composition. As opposed to the EBL, designed to block hot electrons as evident from the term, the electron injector acts as an "electron cooler" by promoting the interaction of ballistic and quasi-ballistic electrons with LO phonons.

6.1. Staircase electron injector (SEI)

Figure 11 shows a schematic of a DH LED with a 2-layer staircase electron injector (SEI) composed of $In_{0.04}Ga_{0.96}N$ and $In_{0.08}Ga_{0.92}N$ layers inserted between the n-GaN layer and the active region ($In_{0.2}Ga_{0.8}N$). Indium contents in the SEI layers are chosen in such a way that each of the 2 steps are greater than the LO phonon energy of 88 meV. Note that the specifics of the SEI region depend on the active layers itself in that

thicker active layers and/or active regions formed of multiple quantum wells would lower the requirements and thinner SEI regions might be acceptable.

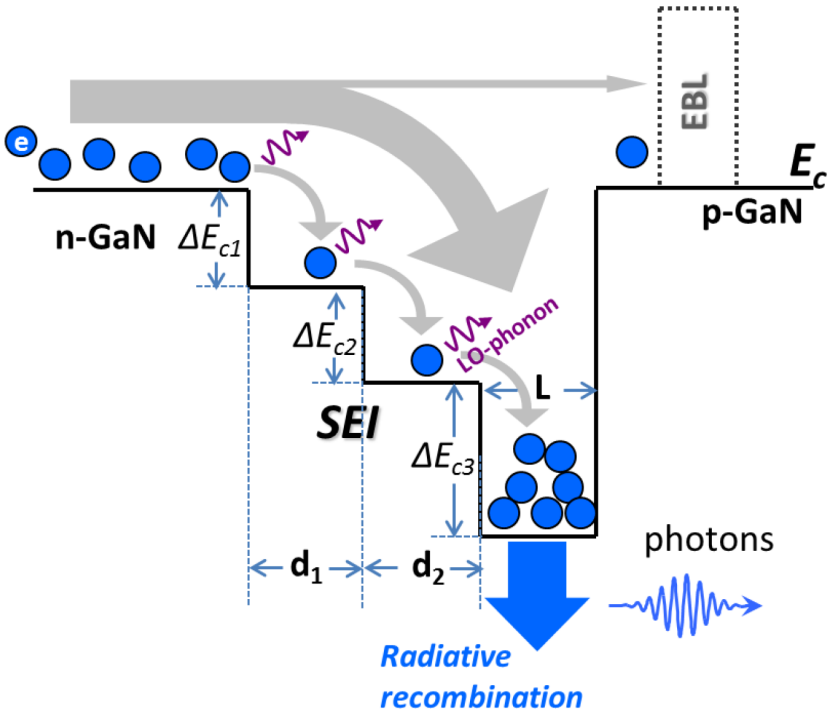

Figure 11. A schematic depiction of the conduction band profile and the enhancement of electron thermalization in the presence of a 2-layer SEI. Recombination in the SEI layers and outside the active region is neglected.

Let us first for simplicity consider cooling of ballistic and quasi-ballistic electrons in a single DH LED with a 1-layer InGaN SEI having an indium composition corresponding to an intermediate bandgap between the n-type electron emitter (n-GaN or n-$In_{0.01}Ga_{0.99}N$ employed in our LED structures) and the InGaN active layer. Since the conduction band discontinuity between the electron emitter and the SEI is smaller than that between the emitter and the active region, the additional kinetic energy and thus velocity acquired by an injected electron are reduced compared to the direct injection from the electron emitter into the active region [72]. As a result the number of scattering events increases as the electrons move slower and spend more time inside the SEI. Therefore, the hot electrons will interact more efficiently with LO phonons and thus thermalize, reducing the electron overflow. The percentage of overflow electrons due to ballistic transport in the LED with a 1-layer SEI is then given by:

$$P_3 = \frac{\int_{\max\{0,(\phi_{EBL}-qV)\}}^{+\infty} f(E)\,N(E)\cdot\exp\left(-\left[d/v_1\left(E+\Delta E_{c1}\right)+L/v_2\left(E+\Delta E_{c2}\right)\right]/\tau_{sc}\right)dE}{\int_0^{+\infty} f(E)\,N(E)\,dE}, \tag{15}$$

where d and L are the thicknesses of and $v_1\left(E+\Delta E_{c1}\right)$ and $v_2\left(E+\Delta E_{c2}\right)$ are the electron velocities in the SEI and the active region, respectively. The energies, ΔE_{c1} and ΔE_{c2}, represent the energy gained by electrons from the conduction band discontinuities upon injection into the SEI layer and then into the InGaN active region, respectively. For the flat band conditions, the electron velocities can be expressed as $v_1\left(E+\Delta E_{c1}\right)=\sqrt{2\left(E+\Delta E_{c1}\right)/m_e}$ and $v_2\left(E+\Delta E_{c2}\right)=\sqrt{2\left(E+\Delta E_{c2}\right)/m_e}$. ΔE_{c1} may vary depending

on the SEI design, but it must be greater than the LO phonon energy. As mentioned before, for simplicity, we assume that the electron transport is normal to the hetero-interfaces.

For electrons experiencing 1 scattering event, a total of 4 different cases, corresponding to emission or absorption of only 1 LO phonon in the SEI and the active regions, can be envisioned. For example, the probability of overflow resulting from only one phonon emission in the SEI is given by

$$P_4 = \left(\int_0^{+\infty} f(E)\,N(E)\,dE\right)^{-1} \int_{\max\{0,(\phi_{EBL}-qV+\hbar\omega_{LO})\}}^{+\infty} f(E)\,N(E) \int_0^d \frac{\exp(-[x/v_1(E+\Delta E_{c1})]/\tau_{sc})}{v_1(E+\Delta E_{c1})\cdot\tau_{em}} \times \exp\left(-[(d-x)/v_1\,(E+\Delta E_{c1}-\hbar\omega_{LO}) + L/v_2\,(E+\Delta E_{c2}-\hbar\omega_{LO})]/\tau_{sc}\right)\cdot dx\cdot dE \quad (16)$$

Eq. (16) takes into account the probabilities for a suitable electron (e.g., with energy ω_{LO} higher than the bottom of conduction band of n-GaN for the case of no EBL and flat-bands) to reach position x $(0 \le x \le d)$ without being scattered, to emit a phonon near x, and to exit the active region without being scattered between x and L. The probability of overflow due to only one phonon emission in the active region is given by

$$P_5 = \left(\int_0^{+\infty} f(E)\,N(E)\,dE\right)^{-1} \int_{\max\{0,(\phi_{EBL}-qV+\hbar\omega_{LO})\}}^{+\infty} f(E)\,N(E) \int_0^d \frac{\exp(-[d/v_1(E+\Delta E_{c1})]/\tau_{sc})}{v_2(E+\Delta E_{c2})\cdot\tau_{em}} \times \exp\left(-[(x-d)/v_2\,(E+\Delta E_{c2}) + (d+L-x)/v_2\,(E+\Delta E_{c2}-\hbar\omega_{LO})]/\tau_{sc}\right)\cdot dx\cdot dE \quad (17)$$

A similar path can be taken to obtain the probabilities for 1-phonon absorption events, which for the sake of space is left to the reader. The contribution of 2 scattering events to the overflow electrons was to a first extent found to be inconsequential ($<1\%$) for the 1-layer SEI of 15 nm in width with 0.25 eV band discontinuities between the n-GaN and the SEI and the SEI and the 6-nm $In_{0.2}Ga_{0.8}N$ active region [72]. As a result, the total electron overflow is then obtained by summing the ballistic and quasi-ballistic (1-phonon processes) contributions.

For the second SEI layer, the product of 6 partial probabilities should be used to calculate the total probability of electron overflow via 1 phonon emission:

1. The probability to find an electron with energy $\hbar\omega_{LO}$ higher than the bottom of the conduction band of the n-type electron emitter ($n-$GaN or n-$In_{0.01}Ga_{0.99}N$ in our case) prior to injecting into the active region (as an example, for the case of no EBL and flat bands);

2. The probability of an injected electron to traverse the first SEI layer of thickness d_1 without being scattered.

3. The probability to travelling the distance $x - d_1$ from the interface between the first and the second SEI layers without being scattered.

4. The probability to emit an LO phonon within the second SEI layer of thickness d_2 at a position between x and $x + dx$.

5. The probability to reach the active region (that is, the position of $x = d_1 + d_2$) without being scattered.

6. The probability to reach the p-type GaN ($x = d_1 + d_2 + L$, where L is the active region thickness) without being scattered.

6.1.1. Optimization of SEI

As mentioned above, for the 1-layer SEI (i.e. 1 InGaN layer with intermediate composition before the active region), a relatively small step height between the conduction band discontinuity between the SEI and n-GaN would result in lower electron velocity in the SEI region and thus increase the probability for thermalization. However, a smaller step height between the n-side and the subsequent InGaN layer would result in larger conduction band discontinuity between the intermediate InGaN layer and the active region to follow. Therefore, the probability of electrons traveling across the active region without recombining would increase. The electron overflow percentiles calculated for a single 6-nm $In_{0.2}Ga_{0.8}N$ DH LED with 1-layer SEI with variable step height, ΔE_{c1}, and thickness, d_1, are summarized in Table. A DH configuration was chosen for simplicity. The reader is referred to Refs. [72] and [74] for further details. It should also be noted that, because the barrier height at the p side decreases significantly with applied voltage the electrons thermalized within SEI would significantly contribute to the overflow current due to the increasing likelihood of ballistic or quasi-ballistic transport across the active region.

Table. Calculated electron overflow percentiles for a one-intermediate layer SEI with varying SEI step height ΩE_{c1} and SEI thickness d_1 under flat band conditions ($V = 0$) for an LED with a 6 nm-thick InGaN active region. The values in parenthesis are for $V = 0.1$ V.

ΩE_{c1} (eV)	d = 3 nm	d = 9 nm	d = 15 nm
0.1	36% (70%)	18% (66%)	11% (61%)
0.2	37% (52%)	18% (38%)	11% (21%)
0.3	39% (51%)	21% (36%)	11% (22%)
0.4	41% (52%)	24% (39%)	13% (26%)
0.5	42% (53%)	26% (42%)	18% (29%)

What can be drawn from data presented in Table, under the flat-band condition (i.e. the net potential drop across the active region $V = 0$), is that the 15-nm-thick SEIs with step heights of 0.1, 0.2, and 0.3 eV all result in an overflow percentile of 11%. Similar results have been reported by Park et al. [77], who calculated an overflow percentile of $\sim$13% for an $In_{0.18}Ga_{0.82}N$ LED structure with a single 13-nm-wide InGaN SEI layer having $\Delta E_{c1} = 0.10$ eV and the band discontinuity between the active region and the p-GaN additional increased by 0.05 eV by inserting an EBL with low Al content. Under a bias corresponding to $V = 0.1$ V drop across the active region, the overflow percentile for the 15-nm-thick SEI having a step height of 0.1 eV increases to 61% due to a significant increase in overflow contribution from the electrons thermalized in the SEI but traversing the active region ballistically and or quasi-ballistically. This notable increase in overflow is caused by lowering of the conduction band of p-GaN to the same level as that of the SEI as a result of the bias. For the same bias condition, the 15-nm SEI structures with step heights of 0.2 eV and 0.3 eV have comparable electron overflow percentiles of 21% and 22%, respectively. Further increase in step height gives rise to slightly increased electron overflow percentile compared to those for 0.2-eV and 0.3-eV steps due to increased electron velocity in the SEI. At higher applied voltages (e.g., $V = 0.2$ V) across the active region, it is expected that 0.3 eV or larger step height will yield a reduced overflow percentile for a certain SEI terrace thickness. The above hypothesis is valid for the 2-layer SEI as well. The second step still should be lower than the p side conduction band to the extent possible, which becomes increasingly difficult under increasing forward bias.

The results presented above suggest that for the 1-intermediate layer SEI case, a sufficiently large step height and a larger SEI thickness will reduce the electron overflow. However, growth related restrictions in

terms of the effect of SEI on the material quality and strain inside the active region [78,79] must also be taken into consideration when optimizing the SEI layer stack. For instance, one should note that the increase in step height of the electron injector means a larger In content, and, therefore, higher strain, increasing the probability of strain relaxation and introduction of defects.

We now turn our attention to the case of the multiple-layer SEI. For a given total SEI thickness and also a given conduction band discontinuity between the active region and the SEI region, more steps within the SEI would result in smaller step heights and thus reduced gained kinetic energy for the electrons from the potential and thus reduced electron overflow, providing that the energy steps are equal to or larger than the LO phonon energy. As noted previously, the particulars of the optimum SEI, such as number of SEI steps, their thicknesses, and energy steps at the interfaces within the SEI as well as between the first SEI step and the n-GaN and the last SEI layer and the p-GaN, would depend on the active region design. We demonstrated that the 2-layer SEI with intermediate layer compositions of $In_{0.04}Ga_{0.96}N$ and $In_{0.08}Ga_{0.92}N$ could significantly reduce the efficiency degradation in blue InGaN LEDs, and eliminate the need for an EBL, which hampers the hole transfer [18,64,80]. In addition, the LED efficiency also depends strongly on the active region design and double heterostructure (DH) active regions have been shown to be more promising than conventional quantum wells due to their 3D density of states [7,80,81]. As we will demonstrate below, in some cases, the LED active region, such as a multi-DH one, can act as a rather efficient electron cooler itself. In the following sections we focus on the advantages of the graded electron injector and the optimization of SEI in the blue DH-based LED variety.

6.2. Graded electron injector (GEI)

A graded structure, see Figure 12, in place of stepwise approximation for cooling the electrons that are being injected is much simpler and should be very effective. The conditions imposed on heterojunction discontinuities in the case of SEI are eliminated entirely as the structure automatically cools electrons when they have sufficient potential energy to emit LO phonons. Moreover, electrons in the graded injector are continuously accelerated in the direction normal to the heterointerface due to the electric field. As in the case of the SEI design, the caveat is that the total thickness along with the active layer would have to be considered in the realm of strain and strain relaxation with its ensuing potential defect generation.

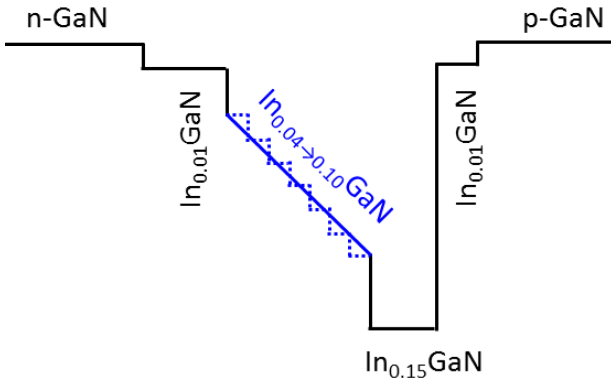

Figure 12. Graded electron injector for cooling the electrons that are injected from the n-side of the junction into the active region, which eliminates design requirements associated with the stepwise graded approach. The dashed lines indicate the step graded approximation, which is indeed the case in actual growth experiments.

Figure 13 compares the electron overflow percentiles calculated for single and quad 3 nm DH LED structures with either an SEI or graded electron injector (GEI). It is clear that the elimination of band discontinuities in the GEI reduces the electron overflow considerably. For single 3 nm DH LEDs, the overflow at 100 A/cm^2 is reduced from 26% with a 4 + 4 nm thick SEI to 12% with an 8 nm thick GEI. These values are reduced to 12% and 10% for a 20 + 20 nm SEI and 40 nm GEI, respectively. For quad 3 nm LEDs, where the thicker active region naturally contributes to electron cooling (see Section 6.3), the overflow at 100 A/cm^2 is reduced from 10% with a 4 + 4 nm SEI to 7% with an 8 nm thick GEI. The corresponding values are 5.5% and 3.5%, respectively, for quad 3 nm LEDs with a 20 + 20 nm SEI and 40 nm GEI. Effects of the electron injector thickness and the active region structure on electron overflow will be discussed further in Section 6.3.

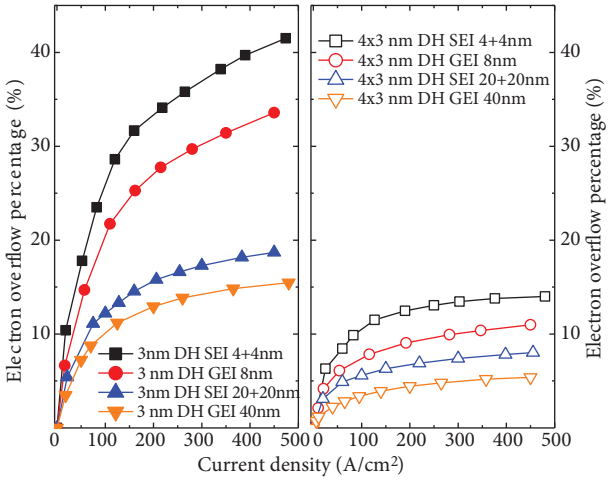

Figure 13. Electron overflow percentiles calculated for (a) single and (b) quad 3 nm DH LED structures with either SEI or GEI of various thicknesses.

6.3. Optimizing electron cooler for a given active region

As stated earlier, the specifics of the SEI region would depend on the specifics of the active region, thicker active regions relaxing the design parameters. In this context, the electron overflow vs. injection current for a variety of single and multi $In_{0.15}Ga_{0.85}N$ DH LEDs with 2-layer SEIs of different thicknesses (with no electron blocking layer) has been calculated. The dependence of efficiency on the active region design will be discussed in Section 8. For simplicity, the electrons are assumed to move in the direction normal to the hetero-interfaces only and, as discussed in Section 4.2, the total electron overflow is obtained by summing the contributions from both ballistic and quasi-ballistic electrons for a given bias voltage [73]. The injected current density vs. bias was obtained using a commercial simulator, Silvaco Atlas, with parameters appropriate for nitride materials as reported in Ref. [73].

Figure 14 shows the schematic (Figure 14a) and the computed electron overflow percentiles (Figures 14b and 14c) for 2 types of LED structures (w/o EBL): (i) single DH LEDs with $In_{0.15}Ga_{0.85}N$ active-region width varying from 3 to 9 nm and (ii) multi-DH LEDs with different numbers of $In_{0.15}Ga_{0.85}N$ active regions separated by 3-nm $In_{0.06}Ga_{0.94}N$ barriers. As evident from Figure 14b, the rate of the electron overflow reduces with increasing active region width. In the absence of an SEI, the overflow percentile for the single 3 nm DH LEDs reaches 68% at $\sim$75 A/cm^2, while only 28% of electrons escape to the p-GaN in the 9 nm DH structure. At 150 A/cm^2 (injection current density beyond that used in general-lighting LEDs), the electron overflow reduces

from 75% in 3 nm to 45% and 32% for the 6 nm and the 9 nm DH structures, respectively. These values are reduced to 31%, 16%, and 10% for the 3 nm, 6 nm, and 9 nm DHs, respectively, when a 4 + 4 nm-thick 2-layer SEI is employed and further to ∼5% with a 20 + 20 nm thick SEI. It should be noted, however, that although the carrier overflow decreases with increasing DH thickness, the use of DH active regions with thickness beyond 6 nm may not be beneficial, because as we will demonstrate shortly it increases nonradiative recombination due to degraded material quality and also substantially reduces radiative recombination efficiency because of poor overlap of electron and hole wavefunctions in wide active regions. Commercial LEDs necessarily feature structures that are optimized considering technological issues as well and rely mainly on multiple quantum wells with thin active layers but cumulatively sufficiently thick active regions.

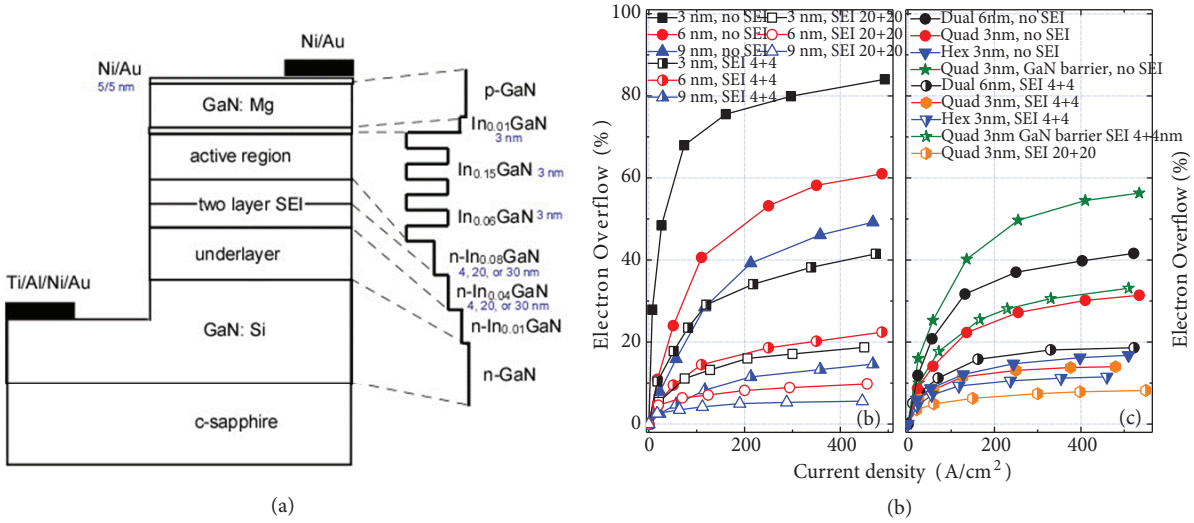

Figure 14. (a) Schematic of the quad 3 nm LED structures investigated. (b) Electron overflow percentile in (b) single DH LEDs and (c) multi-DH LEDs with different SEI thicknesses as a function of injected current density.

Figure 14c illustrates that the thick cumulative active region naturally provides efficient electron cooling. Moreover, when the band offset between the electron emitter (n-GaN or n-$In_{0.01}Ga_{0.99}N$ in our structures) and barriers in the active region becomes larger than the LO phonon energy of 88 meV (i.e. the In content of the order of 4 at. % or higher), the electron-thermalization efficacy increases greatly because the whole active region inclusive of the barriers works in unison as an electron cooler. Owing to the relatively small conduction band discontinuity between the $In_{0.06}Ga_{0.94}N$ barriers and the $In_{0.15}Ga_{0.85}N$ active layers, the reduced barrier heights do not simply contribute to the electron thermalization, but also lower the velocity of electrons entering the active regions, which is beneficial. As evident from Figure 14c, the electron overflow percentile in the quad 3 nm DH without SEI or EBL decreases from 28% to 16% at 75 A/cm^2 when $In_{0.06}Ga_{0.94}N$ is used as the barrier material instead of GaN and from 56% to 31% at 500 A/cm^2.

Short period superlattices (SLs) as electron coolers/injectors have also been proposed by several groups [77,82]. The SLS electron injector proposed by Park et al. [77] utilizes barriers with 100 meV band offset between n-GaN and InGaN barriers on the n-side of the junction. The salient feature of our active-region design is that the cooling of ballistic and quasi-ballistic electrons is very efficient inside the active region, and, therefore, the requirements for additional electron cooling prior to entering the active region may be relaxed to some extent.

6.3.1. Experimental data

Single and multi-DH LEDs with 4 + 4, 20 + 20, or 30 + 30 nm-thick 2-layer SEIs ($In_{0.04}GaN$ + $In_{0.08}GaN$), schematically depicted in Figure 15a and theoretically discussed above, were fabricated and analyzed. The c-plane InGaN LED structures, emitting at ∼430 nm, were grown on ∼3.7 μm-thick Si-doped n-type GaN templates on sapphire in a vertical low-pressure metalorganic chemical vapor deposition (MOCVD) system. Situated below the active region is a 2-layer varied thickness SEI grown on a 60-nm n-type (2×10^{18} cm^{-3}) $In_{0.01}Ga_{0.99}N$ underlying layer. The SEI structure consists of $In_{0.04}GaN$ and $In_{0.08}GaN$ layers of the same thickness grown in the given order. The LED structures were terminated with 100 nm-thick Mg-doped p-GaN layers having 6×10^{17} cm^{-3} hole density. Square mesa patterns (400×400 μm^2) were then formed by chlorine based inductively coupled plasma (ICP) etching. Ti/Al/Ni/Au (30/100/40/50 nm) metallization annealed at 800 °C for 60 s was used for n-type ohmic contacts, and 5/5-nm Ni/Au electrodes served as the semitransparent p-contacts with 40/50-nm Ni/Au electrodes deposited for p-contact pads, which completed the LED fabrication.

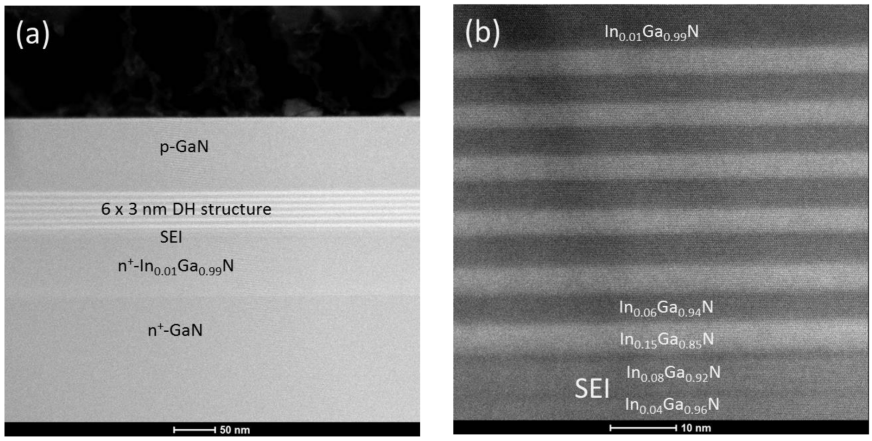

Figure 15. (a) Cross-sectional STEM image of the hex 3 nm DH structure. Neither extended defects nor indium clusters are seen within the viewing field. (b) An enlarged image of the active region. Image courtesy of Dr A Kvit and Prof P Voyles.

A high-resolution scanning transmission electron microscopy (STEM) micrograph of a 6×3 nm DH LED is presented in Figure 15, indicating the high crystallinity and sharp interfaces of the MOCVD-grown structures. These images together with those in the literature clearly indicate that there is no visible In clustering, at least for blue emitters. While this dispels the arguments used ubiquitously for accounting for many maladies associated with InGaN-based structures, the same cannot be used to rule out localization due to electronic defects. With improved quality, as evidenced in commercial LEDs with only <2 nm variation in the emission wavelength across a 200 mm wafer (discounting the normal edge effects) [83], the In fluctuations or the compositional inhomogeneities are now a moot point, again at least for the blue emitters, albeit there exists atomic steps on the upper surfaces of InGaN [84]. Defective materials and also emitter structures at longer wavelength may exhibit compositional inhomogeneities.

To experimentally verify the overflow predictions, the integrated electroluminescence (EL) intensity vs. current injection for single 3 nm and 6 nm DH LEDs and quad 3 nm DH LEDs chips with varied SEI thickness was measured (0.1% duty cycle and 1 kHz to eliminate heating effects). Care was taken to assure invariance

in the light collection geometry among all the chips tested. Moreover, the light emission intensity showed less than 5% variation among at least 5 devices measured on the same wafer.

Figure 16a demonstrates that for the LEDs with a 4 + 4 nm SEI, the EL efficiency of the quad 3 nm DH LED is ∼3.5 times higher than that of single 3 nm DH LED. This is in agreement with the calculated electron overflow percentiles shown in Figures 14b and 14c predicting substantially higher overflow for the single 3 nm DH LED. One can then draw the conclusion that the low EQE of the single 3 nm DH structure is due to higher carrier overflow in the thinner active layer facilitating ballistic and/or quasi-ballistic electron transport across the active layer without recombination [73]. The SEI thickness should be larger for single 3 nm DH to provide hot electrons more time to sufficiently thermalize before being injected into the active region. However, regardless of the active layer design, the total SEI thickness must be kept below the critical thickness above which the active region material quality would degrade noticeably due to strain relaxation. It should also be noted that the agreement between the simulation results of Figure 14 and the data presented in Figure 16 is satisfactory considering that the calculations assume a constant phonon scattering rate, which would result in underestimation of the overflow percentiles as the phonon lifetime has been reported to decrease with increasing electron density (current injection) [85].

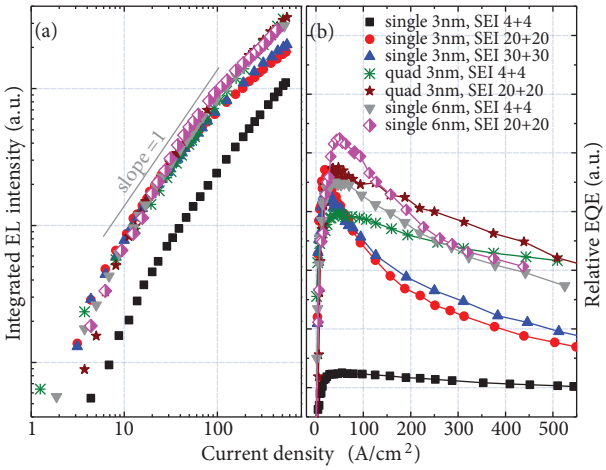

Figure 16. (a) The integrated EL intensity dependence on current density for single and quad 3 nm DH LEDs with varied SEI thickness. (b) The relative EL efficiency vs. injected current density.

Increase in the SEI thickness from 4 + 4 nm to 20 + 20 nm for the single 3 nm DH LED resulted in an enhancement in the peak EL efficiency by nearly 3.5 times, making it comparable to those of the quad 3 nm DH LEDs (Figure 16a) and the single 6 nm DH with 4 + 4 nm SEI. This significant improvement indicates that the electrically injected hot electrons are cooled more efficiently within the thicker SEI. The more visible efficiency roll off in the single DH LED both with 20 + 20 and 30 + 30 nm-thick SEIs compared to the single 6 nm and the quad 3 nm DH LEDs (Figure 16b) suggests larger electron overflow in the thinner active region, which increases at higher injection levels. At the highest injection level employed (550 A/cm^2, which corresponds to an average carrier density around 5×10^{18} cm^{-3}, estimated using A = 10^7 s^{-1} and B = 10^{-10} cm^{-3} s^{-1}) [86], the efficiency for the single 3 nm DH LED with 20 + 20 nm SEI is nearly twice that for the single DH LED with 4 + 4 nm SEI and 55% to 70% of those for single 6 nm and quad 3 nm DH LEDs. Note that thicker, multi-DH or MQW active regions would serve as efficient electron coolers. Accordingly, the single 6 nm DH and the quad 3 nm DH LEDs with 20 + 20 nm SEI show only a moderate increase of 15%–20% in the peak

EQE compared to those for the LEDs with 4 + 4 nm SEIs. At injection current densities below 200 A/cm^2 (the range of the practical interest for LED applications), the quad 3 nm DH and the single 6 nm DH with 20 + 20 nm SEI show higher relative EQE values due to the reduced overflow as compared to their counterparts with 4 + 4 nm SEIs and retain about 87% and 79% of their peak EQEs at 150 and 200 A/cm^2, respectively.

To demonstrate further that the loss of efficiency at high injection is due to carrier overflow, the single and quad 3 nm DH LED structures were investigated under resonant optical excitation. The data shown in Figures 17a and 17b also demonstrate that the PL intensity nearly scales with the number of 3 nm active layers.

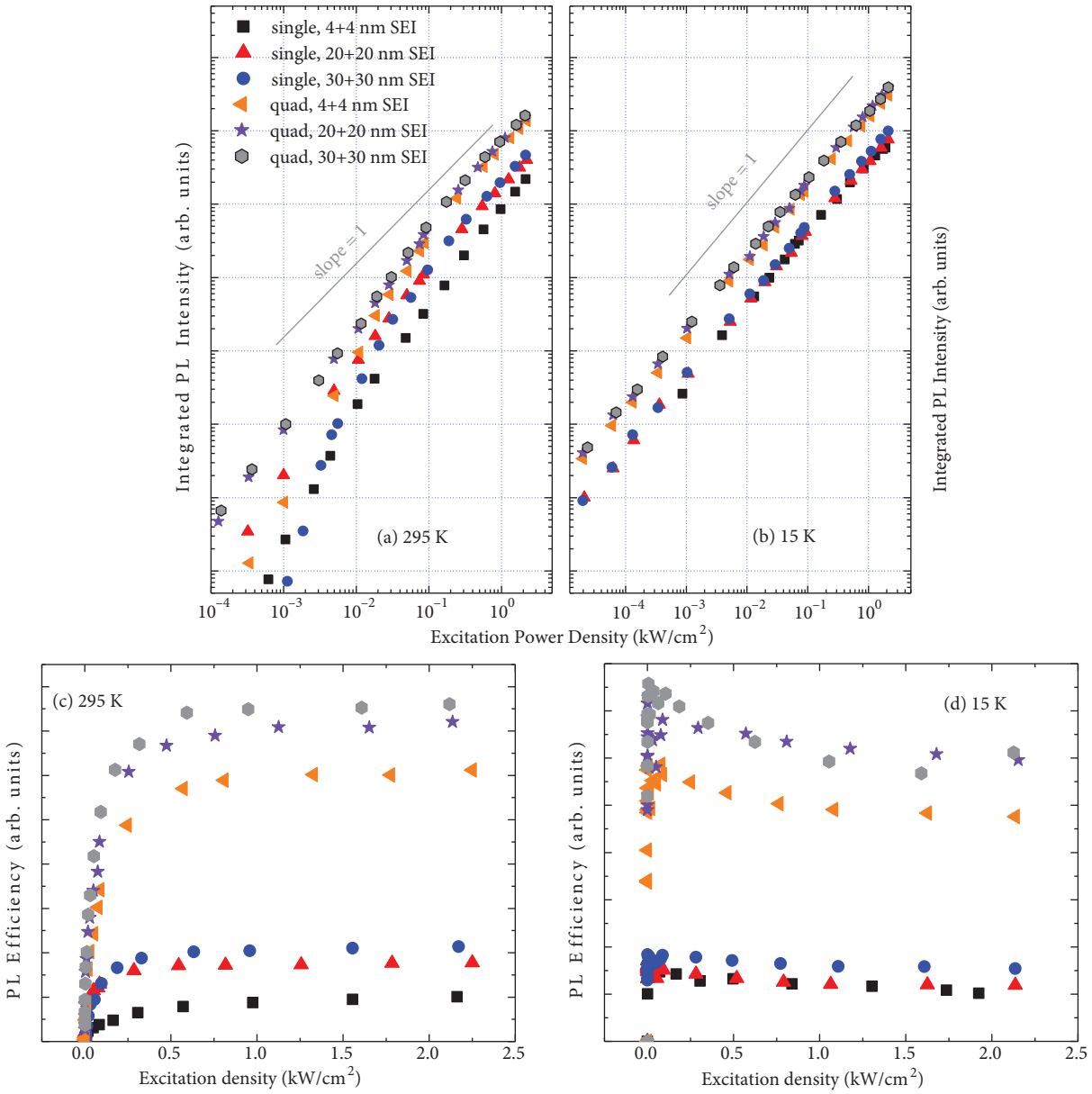

Figure 17. The integrated PL intensity dependence on optical excitation density at (a) 15 K and (b) 295 K for single and quad 3 nm DH LEDs with varied SEI thickness. (c) and (d) show the corresponding PL efficiencies. The legend in (a) applies to all figures.

The variation in intensity with SEI thickness is due in part to unintentional variations in the active layers thickness, absorption in the SEI layers, and improvement in the active layer quality with the underlying SEI. The reduced slopes of the PL intensity versus excitation density plots in the relative low-excitation regime for LEDs with thicker SEIs are also supportive of the latter. Nevertheless, the room temperature PL efficiencies shown in Figure 17c do not exhibit any drop with increasing optical injection up to the maximum excitation density used. While the drop is evident at 15 K for the quad DH LEDs (Figure 17d), the PL efficiency is retained with further increase in injection, at power density exceeding 1 kW/cm^2.

7. Injection-dependent radiative recombination coefficient (B) of single and multi active layer DH LEDs

The radiative recombination coefficient, B, is dependent on injection through a variety of processes. Change in junction temperature due to Joule losses is one such process as the B coefficient is inherently temperature dependent. Carrier lifetime, which is related to the B coefficient, increases with temperature, which implies that the B coefficient decreases with increasing junction temperature exacerbated by limitations in heat transfer [87]. The B coefficient is also dependent on injection due to the skewed band edges in the active region of LEDs and also on the total number of states that are available. In biaxially strained InGaN/GaN layers, the mismatch strain induces a polarization field (caused by the lack of centro-symmetry in wurtzite lattice) along the growth direction in layers grown on the basal plane [88]. In LEDs based on DHs, this strain-induced piezoelectric field and spontaneous polarization field skew the potential profile, resulting in triangular potential profiles near the hetero-interfaces of active regions. The simulated potential profiles, using the commercial Silvaco Atlas software package, are shown in Figures 18a and 18b for 3 nm and 9 nm DH LEDs, respectively, at different injection current densities. Note that a factor of 0.4 was used for the polarization induced charge for both electrons and holes at the interfaces in generating Figure 18a. The reasons behind this apparently arbitrary choice will receive some discussion farther down the line. In a thick active layer (Figure 18b), electron and hole wavefunctions are widely separated at low injection levels, which results in reduced radiative recombination rate and relatively low relative EQE. Furthermore, at low injection levels, the available states of this triangular potential well are not completely filled. However, upon increasing the injection level the triangular region will be fully occupied due to the relatively low density of states. With a further increase in injection, the quasi-continuum states followed by the 3 dimensional states in the DH active region will begin to fill, leading to a higher recombination rate and thus higher relative EQE. Moreover, a blue-shift, whose magnitude depends on the active layer thickness, occurs with increasing current injection [89].

Figure 18c shows the experimental peak emission energy shift as a function of injection current density from electroluminescence (EL) measurements performed on LED structures with varied DH thickness. Naturally, relatively large peak energy shifts are observed with injection when the DH thickness is increased from 3 nm to 9 nm. For single 6 nm, dual 6 nm, and single 9 nm DH LEDs, a significant 25 meV energy shift is observed with injection increasing from 0 A/cm^2 to 40 A/cm^2, while only a 8 meV shift is evident for the 3 nm DH LED within the same current density range. Figure 18d shows the simulated peak energy shift vs. the current density wherein polarization charge densities of 7.7×10^{12} cm^{-2} and 3.8×10^{12} cm^{-2} have been used for the interfaces between the $In_{0.01}Ga_{0.99}N$ barrier and the $In_{0.15}Ga_{0.85}N$ active layer, and the $In_{0.15}Ga_{0.85}N$ active layer and the $In_{0.08}Ga_{0.92}N$ SEI, respectively. These are fractions (0.4) of the theoretical values [90] and provide energy shifts that are in reasonable agreement with experiments (Figure 18c). We should note that varying the polarization charge in the simulations changes the absolute energy shift, but does not affect the

peak energy shift dependence on the active layer thickness. The substantial reduction in the energy shift when the DH thickness is further increased to 11 nm is most probably due to partial strain relaxation of the InGaN active layer, which is not considered in the simulation software.

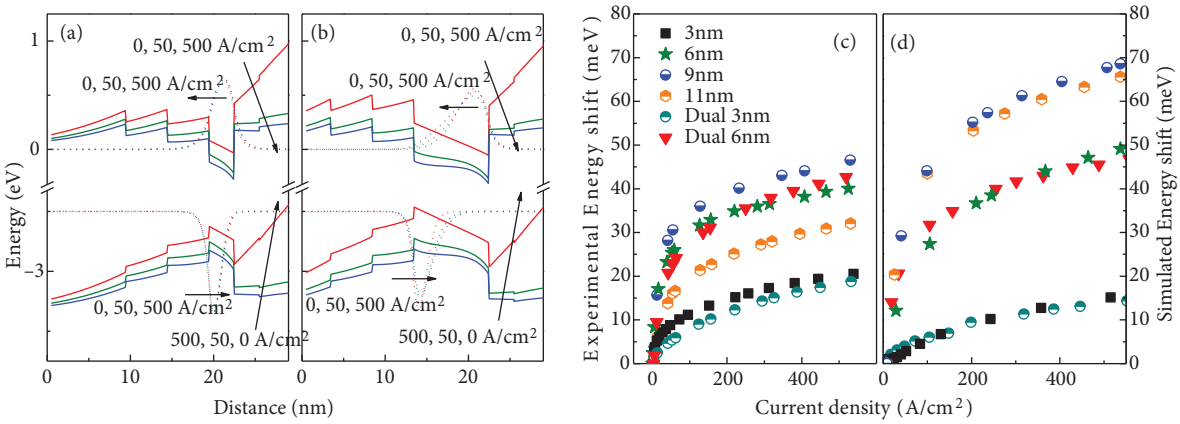

Figure 18. Energy band edge profiles simulated for (a) 3 nm DH and (b) 9 nm DH LEDs with 4 + 4 nm SEIs at different injection current densities. Peak emission energy shift as a function of injection current density from (c) EL measurements and (d) Silvaco simulations for DH LED structures with various active regions. The same legend is used for (c) and (d).

We now discuss the electron and hole wavefunction overlap in the context of radiative recombination coefficient as a function of injection current density for active regions composed of single and multiple DHs of various widths. The change in the effective radiative coefficient B_{eff} is dependent on the active layer design. In this context, relying on the EL and resonant PL data, we show that the relative EQE increases considerably by increasing DH active layer thickness from 3 nm to 6 nm. At high injection, the relative EQE can be enhanced further in multi 3 nm DH and 6 nm DH LEDs, separated by 3 nm-thick $In_{0.06}Ga_{0.94}N$ barriers. Incorporating more DH active regions of the same thickness, separated by thin and low InGaN barriers, ameliorating carrier (particularly hole) transport across the active region, results in enhanced emission intensity without any discernible degradation of the active region quality unlike that observed in thicker single DH layers due to strain relaxation with increasing InGaN thickness [80]. We find that employment of low and thin InGaN barriers is essential for ameliorating carrier (particularly hole) transport across the active region.

Detailed derivations of injection dependent radiative recombination coefficient can be found elsewhere [80]. Here we will discuss briefly only the most essential steps of the calculations. Let us consider a system with confinement along the z-direction (growth direction). Following the formalism of Ref. [91], the rate of spontaneous transition from a group of initial states i in the conduction band to a group of final states f in the valence band separated by a transition energy $\hbar\omega$ can be expressed in the realm of Fermi's golden rule as:

$$K_{i\to f} = \left(\frac{eA_0}{2m_0}\right)|M|^2\left|\int \psi_f^*(z)\psi_i(z)dz\right|^2 \rho_r(\hbar\omega)F(\hbar\omega) \tag{18}$$

where A_0 is the magnitude of the sinusoidal local vector potential, e is the electron charge, m_0 is the free electron mass, M is the in-plane momentum matrix element, $\rho_r(\omega)$ is the reduced density of states, ω is the transition energy, $F = f_c(1-f_v)$ is the Fermi factor given in terms of the Fermi functions for the conduction

(f_c) and valence bands (f_v), $\Psi(\mathbf{r}) = \psi(z)\,\phi(\mathbf{r}_{xy})$ are the envelope functions representing the wavefunctions. As noted in Eq. (18), the spatial overlap between the electron and hole wavefunctions (ψ_e and ψ_h) is obviously imperative, and the radiative recombination rate is proportional to the square of overlap integral when electrons and holes are confined in the $z-$direction.

To circumvent the artificial dependence of the radiative recombination current on size in structures with quantum confinement, low-dimensional equivalents of the B coefficient are introduced [91]. By defining the spontaneous transition rate as $T_{spont} = B_{2D} n_{2D} p_{2D}$, where n_{2D} and p_{2D} are the 2D electron and hole densities, respectively, the 2D B coefficient in InGaN quantum wells with confinement along the z-direction can be expressed in terms of the momentum matrix element of Eq. (18) (Ref. [91]):

$$B_{2D} = \frac{4\pi n\hbar^2}{\varepsilon_0 c^3 k_b T}\frac{(\hbar\omega)}{m_e^* m_h^*}\left(\frac{e}{2m_0}\right)^2 \times |M|^2 \left|\int_0^\infty \psi_h^*(z)\psi_e(z)dz\right|^2 \rho_r(\hbar\omega), \tag{19}$$

where n is the refractive index, ε_0 is the permittivity of free space, c is the speed of light, $\hbar\omega$ is photon energy, $k_B T$ is the thermal energy, and m_e^* and m_h^* represent the electron and hole effective masses (attainable through linear interpolation from the binary end points for a given In content). The momentum matrix element M can be obtained from the in-plane interband transition matrix element (for polarization within the plane), $P_{cv} = 2\,|M|$ [92], which has been determined from the absorption measurements for binary constituents InN and GaN [93]. Using $P_{cv} = 9.6 \times 10^{-20}$ g cm/s obtained from linear interpolation for the required composition, we calculated the B_{2D} coefficient to be 1.8×10^{-4} cm^2 s^{-1} for an $In_{0.15}Ga_{0.85}N$ active region assuming full overlap of electron and hole wavefunctions. For 3D rate equation, applicable to 3D DH structures, the 2D B coefficient should be multiplied by the active region thickness, L_z. To test this approach and the validity of the 2D approximation, the 3D limit for the B coefficient for $In_{0.15}Ga_{0.85}N$ was also calculated from the following equation (Ref. [94]):

$$B_{3D} = \frac{e^2}{m_0^2 c^3 \hbar^2}\left(\frac{2\pi\hbar^2}{k_B T}\right)^{3/2} \times M^2 \times \frac{1}{\overline{m}_x \overline{yz}^{1/2}}\hbar\omega, \tag{20}$$

where $\bar{m}_{x,y,z} = m_{e(x,y,z)} + m_{h(x,y,z)}$. The value of 3D B coefficient derived from Eq. (20) is 5×10^{-11} cm^3 s^{-1} for $In_{0.15}Ga_{0.85}N$. This value is smaller than that obtained using $B_{2D}L_z$ even for the thinnest active region with $L_z = 3$ nm investigated in this study. We, therefore, assume that all LEDs with active region widths of 3 nm and above exhibit 3D behavior but with an electric field along the growth direction reducing the spatial overlap of charge carrier distributions in the active region. Therefore, the injection dependent overlap integral of the electron and hole wavefunctions should be incorporated into the calculation of the 3D B_{eff} coefficients using 5×10^{-11} cm^3/s as the upper limit for full overlap:

$$B_{eff} = \left(5 \times 10^{-11}\right)\left[cm^3 s^{-1}\right] \times \left|\int_0^\infty \psi_h^*(z)\psi_e(z)\,dz\right|^2 \tag{21}$$

Discussed next are the effects of the active region design and the resulting polarization-induced field [95] on the overlap integral and the associated spontaneous recombination rates in InGaN structures with QWs and DH at different injection levels. Figure 19 represents the simulated bimolecular recombination coefficients, B_{eff}, derived from the transition matrix element and thus the simulated squared overlap integrals of the electron and hole wavefunctions in the single and multi DH active regions. Note that the calculated B_{eff} coefficients may vary

slightly based on the material parameters used; however, this would not alter the major trends. It is apparent from Figure 19 that the radiative recombination coefficient, instead of being constant as assumed in Ref. [96], in fact depends on injection and particulars of the active-region [97]. The B_{eff} coefficient initially increases with injection and then tends to saturate at high injection levels as the flat band condition is approached [95]. Thinner active layers have larger spatial overlap of the electron and hole wavefunctions and thus a faster increase rate of radiative recombination coefficient B_{eff} with injection as well as larger B_{eff} values at low injections (Figure 19a).

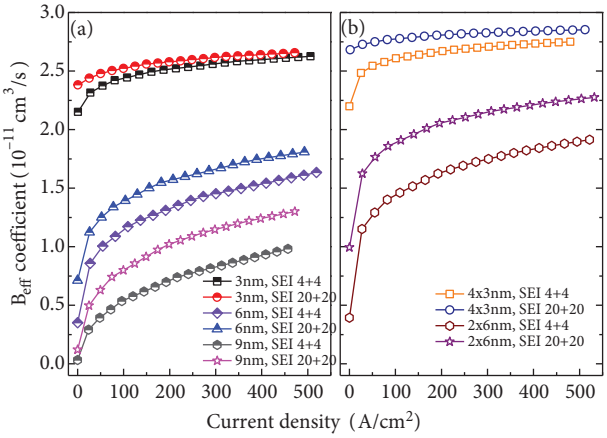

Figure 19. Calculated coefficients B_{eff} of (a) single DH, and (b) multi DH LEDs, calculated using squared overlap integrals of electron and hole wavefunctions (proportional to radiative recombination rate) within the active region as a function of current density using the Silvaco Atlas software package. The SEI layer thicknesses are provided in the legends in nm units.

At $\sim$200 A/cm^2, the single 3 nm DH LEDs exhibit about 37% and 61% higher squared overlap integral value compared to the single 6 nm and the single 9 nm DH LEDs, respectively. The change in the B_{eff} coefficient with injection is very small for the single 3 nm DH LEDs, while that for wider DHs exhibits a substantial increase in B_{eff} coefficient within injection in the range of 0 A/cm^2 to 500 A/cm^2. The smaller B_{eff} coefficients in wider active regions are, naturally, attributable to increased spatial separation of electrons and holes caused by the polarization fields.

It is worth noting that wider SEIs give rise to larger overlap integrals for otherwise the same active layer thickness. The same holds for wider active regions as well. The calculations show around 7% higher B_{eff} for the dual 3 nm DHs with both 4 + 4 nm and 20 + 20 nm SEIs compared to the single-DH variety at 100 A/cm^2. At 500 A/cm^2, the corresponding values for the dual DH LEDs with 4 + 4 nm and 20 + 20 nm are 5% and 6%, respectively. The difference in the overlap integrals for the single and the dual 6 nm DH LEDs is larger, exemplified by the dual structures with 4 + 4 nm and 20 + 20 nm SEIs exhibiting 18% and 22% larger B_{eff} coefficients, respectively, at 100 A/cm^2. When injection approaches 500 A/cm^2, this difference is somewhat reduced to 13% and 20% for the LEDs with 4 + 4 nm and 20 + 20 nm SEIs. However, as seen in Figure 19b, a further increase in the number of 3 nm DH active regions from 2 to 4 only slightly increases the overlap integrals.

8. Effect of the active region design on the LED efficiency

As illustrated in the previous section, the wide DH or the multi-DH active region LED design enhances the thermalization of hot electrons, which reduces carrier overflow. The same naturally applies to MQW active regions with more periods. However, the reduced electron overflow alone is not sufficient to produce high-brightness LEDs. The optimum design of the active region should be accompanied by high radiative recombination coefficient B and low nonradiative recombination coefficient A, the latter is related to the presence of point and extended defects in the active region. In the event the Auger process is in play, then a small C coefficient would be desired. It should be noted, however, that the Auger process is of intrinsic origin unless defects are involved.

In the case of MQW LEDs, at first glance and in the absence of any technological constraints, the increase in the number of QWs in the active region is the most straightforward approach for efficiency retention. However, due to the poor hole transport, light would be expected to be emitted primarily from the QWs closest to the p-GaN [98–100]. As a result, the peak EQE reaches the maximum rapidly and further increases in bias voltage would cause electron overflow and rapid efficiency loss. This problem can be partially mitigated by employing coupled QWs, that is multiple QW-active regions separated by barriers sufficiently thin to allow the electron and hole wavefunctions to leak through. Relatively thin (3 nm) and low InGaN barriers ($In_{0.06}Ga_{0.99}N$) in the MQW active region would improve the transport of holes. Additionally, as discussed in the previous section, relatively low barriers (still $>$ LO phonon energy below the electron emitter band edge) also enhance cooling of hot electrons while maintaining high quantum efficiency. However, the limited 2D density of states (DOS) in MQW active regions may still cause the EQE to decrease with further rises in the injection current density unless the cumulative active region is sufficiently thick, keeping in mind the compromise that would have been made with self-absorption.

An alternative approach to MQWs is to use DH active regions ensuring uniform carrier spreading across the active region owing to high 3D-like density of states [7]. Among the ramifications of DH are the degradation of InGaN quality and the increased band bending due to any polarization field causing large spatial separation of electron and hole wavefunctions. The latter results in relatively slow EQE increase rates with injection current compared to the MQW-LED as expected. Effectively, due to partial screening of the electric field, the radiative recombination coefficient increases with injection current before other ailments set in. To avoid confusion with the radiative recombination coefficient describing the fundamental properties of a material, this injection-dependent parameter can be dubbed as the effective radiative coefficient, or B_{eff}, discussed in Section 7. When all the above-mentioned factors on the active layer material quality and the radiative efficiency are taken into consideration, the active regions composed of 3D or quasi-3D multi-DH active layers separated by low and thin barriers emerge as the natural choice as will be discussed below.

8.1. IQE and EQE of single and multi active layer DH structures

To evaluate IQEs of the LED structures, excitation density dependent resonant photoluminescence (PL) experiments were conducted at 15 K and room temperature for single and quad DH LEDs with varying SEI thickness with the aid of a frequency-doubled Ti:Sapphire laser (385 nm wavelength) to ensure excitation of the DH active regions only [11,65]. Because carriers under resonant excitation are confined inside the active region already, the overflow effect is eliminated in the optical experiment. Assuming the IQE of InGaN DHs is 100% at helium temperatures, the PL intensity should be proportional to total thickness of the DH layers in the active region. This is a good assumption [101] because, as shown in Figure 20, the observed emission intensity vs. excitation

exhibits a unity slope for excitation powers exceeding approximately 10^{-3} kW/cm^{-2} and 10^{-1} kW/cm^{-2} at 15 K and 300 K, respectively. At very low excitations, the PL intensity vs. excitation power deviates from linearity due to the contributions from defect-related nonradiative recombination and excitation-dependent B_{eff} coefficient. This effect is more pronounced in wider DH active regions featuring both a stronger dependence of radiative recombination coefficient and also a larger probability of strain-driven defect generation.

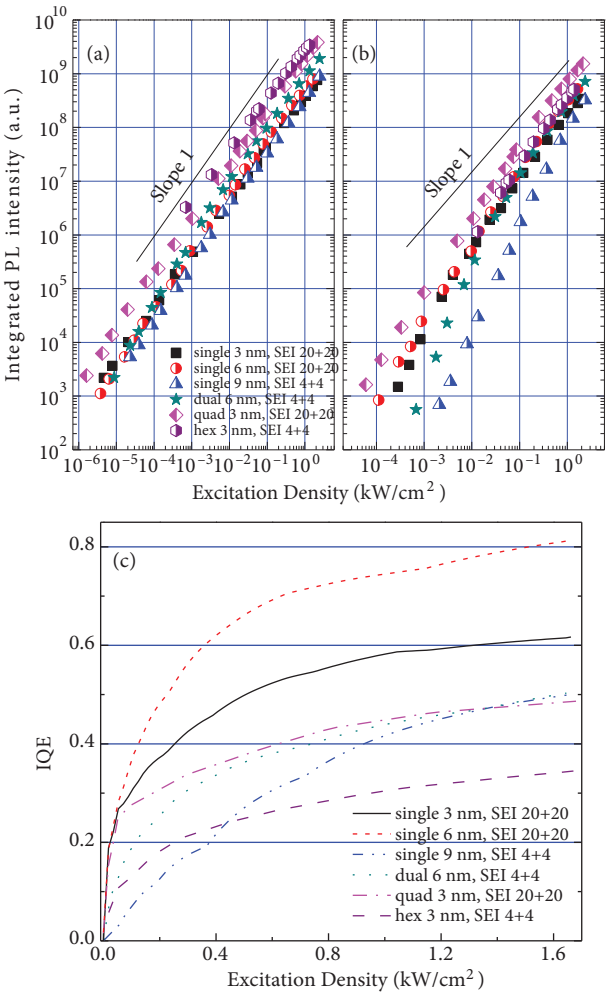

Figure 20. Integrated PL intensities of single and multi DH LED structures as a function of excitation power density measured at (a) 15 K and (b) 300 K. (c) IQEs of the LEDs as a function of excitation power density calculated as a ratio of room-temperature to 15-K PL intensity.

Using $A = 10^7$ s^{-1} and $B = 5 \times 10^{-11}$ cm^{-3} s^{-1}, an injected carrier density at the maximum excitation density employed is estimated to be approximately 2×10^{18} cm^{-3} in the single 3 nm DH LED structure. Note that one should correlate with care the results of IQE measurements with optical excitation and EL data obtained with electrical injection. Under resonant optical excitation, changes in the band bending caused by polarization fields are induced entirely by the presence of photo-generated carriers in the active region, while there is a significant change in the band structure under electrical excitation even before the onset of current flow. The latter changes significantly the overlap of electron and hole wavefunctions. As seen in Figure 20a, the low-temperature PL intensity scales with the number of 3 nm DH layers or the total thickness

of the active region fairly well in that the PL intensity for quad DH LEDs is about 4 times that of single DH LEDs. Consistent with the overall active region thickness, the PL intensities from the 6 nm DH LED structures are between those for single 3 nm DH and quad 3 nm DH LEDs. However, due to excitation dependent overlap integrals (see simulations in Figure 19), the integrated PL intensities from the single-DH active regions do not scale with thickness. At room temperature, the LED structures with the thickest cumulative active regions (dual 6 nm and hex 3 nm DH LEDs) show lower PL intensities (Figure 20b). The PL intensity of dual 6 nm DH structure is virtually equal to that of single 6 nm DH LED, while the hex 3 nm DH exhibits even weaker PL intensity than the thinner quad 3 nm DH structure. These structures have the highest probabilities for strain-driven defect formation. One should note that, because light absorption in DH structures is also proportional to the overlap of electron and hole wavefunctions, the same excitation power density would produce different densities of photo-excited carriers in DH active regions of different thickness.

Figure 20c represents IQE values assumed to be the ratio of room-temperature and 15-K PL intensities for the single- and multi-DH structures as functions of the excitation density. Note that the IQE of none of the LEDs is saturated even at the highest excitation power employed in this study. Among the structures studied, the single 3 nm and the single 6 nm LEDs exhibit the highest IQE values of $\sim$60% and 80% at high excitation levels, respectively. The 9 nm DH LED shows the slowest IQE rate of increase at low excitations; however, its IQE increases at the highest rate at high excitations, which is likely due to the excitation-dependent increase of B_{eff} coefficient (see data shown in Figure 19a). The slow IQE rise in this structure at low excitations can be attributed to nonradiative recombination centers rather than the excitation-dependence of the radiative recombination efficiency. The dual 6 nm DH structures exhibit slower initial IQE increase rates compared to its single-DH counterpart (but higher than the single 9 nm DH), while the calculated B_{eff}, shown in Figure 19, points to a comparable IQE rise rate for the dual DH and single 6 nm DH structures. At high excitations, the dual 6 nm DH LED shows an IQE increase rate higher than that of the 9 nm DH and approaches an IQE of 55%. The IQE of the quad 3 nm DH LED increases with the excitation power at the same rate as those for the single 3 nm and the single 6 nm DHs for low excitations, but its dependence on the excitation power is shallower than those for the single 3 nm, single 6 nm, and the dual 6 nm DH LEDs. At high excitations, the IQE of the quad 3 nm DH reaches about 50%. The IQE of the hex 6 nm DH LED increases with excitation power with a rate very similar to that of the 9 nm DH structure. At high excitations, this structure shows the slowest IQE rise and reaches only 35%. As alluded to above, the hex 3 nm DH structure has the largest total thickness of the active region among all the structures investigated; therefore, it has the highest probability of defect generation caused by strain relaxation.

As noted, resonant optical excitation ensures uniform electron and hole generation in the active region, which is also void of carrier overflow induced efficiency degradation observed under electrical injection. Moreover, the presence of some moderate amount of nonradiative recombination centers in the active region evidently affects the integrated PL intensities in the low excitation regime. While the true nature of recombination centers is used in deriving the rate equation, albeit with many approximations, this term is also used generically in the context of other nonradiative centers, which can be saturated under high excitation, both electrical and optical.

As displayed in Figure 21a, the measured EQE of the 3 nm DH LED increases at a fast rate with injection and reaches its maximum at $\sim$18 A/cm^2 owing to the greater spatial overlap of electron and hole wavefunctions. The 6 nm DH LED exhibits a slightly slower EQE rise rate and peaks at $\sim$41 A/cm^2 (Figure 21a). However, its maximum EQE is about 11% higher than that of the 3 nm DH structure, most likely due to

its higher IQE (see Figure 20b) and/or larger total number of states afforded by the 6-nm InGaN active layer as compared to the 3-nm InGaN layer. The 9 nm DH LED shows a slow rise of EQE with increasing injection current and reaches its maximum EQE at the injection current density as high as 220 A/cm^2 (Figure 21a). The maximum EQE value in this structure is lower than those in the 3 nm and the 6 nm DHs by 11% and 20%, respectively. The slow initial EQE rise in the 9 nm DH is likely caused by both defects and slow increase in B_{eff} coefficient with injection current (Figure 19a). The relatively low maximum EQE can be ascribed to: (i) low value of radiative recombination coefficient because of wide separation of electron and hole wavefunctions, and (ii) possible onset of strain relaxation giving rise to enhanced nonradiative recombination. Increase in DH active region width to 11 nm results in a further decrease in the maximum EQE and even slower EQE rise with injection current density. The 9 nm DH LED shows the highest EQE among the single DH LEDs studied at injection current densities above ~180 A/cm^2 with small efficiency degradation (~10% at 500 A/cm^2 with respect to the maximum).

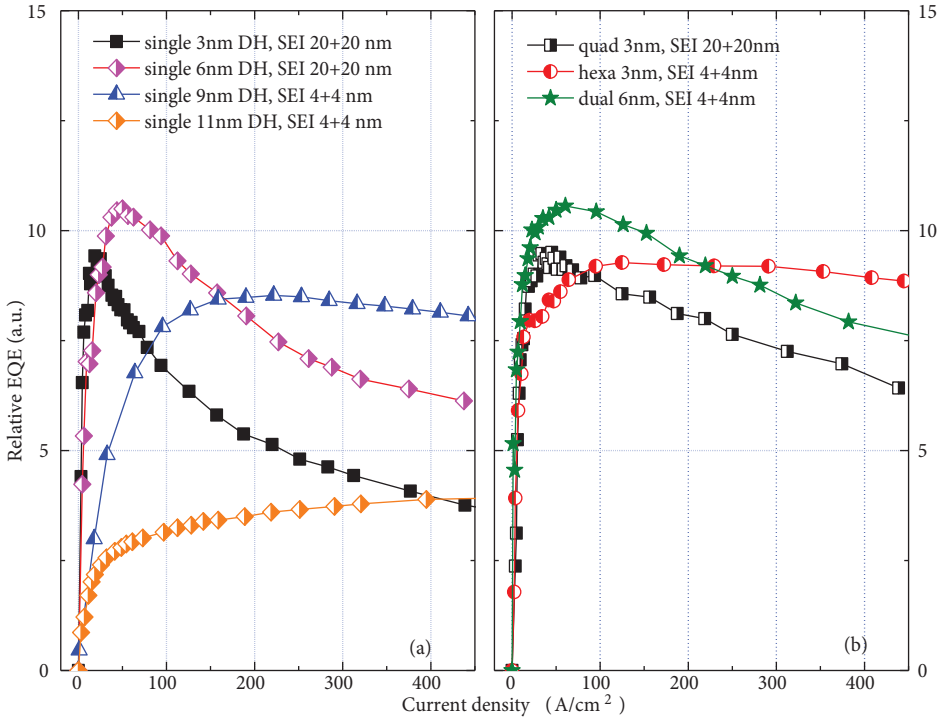

Figure 21. Relative EQEs measured for (a) single DH and (b) multiple DH LEDs as a function of pulsed injection current density (0.1% duty cycle and 1 kHz frequency).

The quad 3 nm DH and the dual 6 nm DH LEDs with 3 nm $In_{0.06}Ga_{0.94}N$ barriers show virtually the same EQE maximum values as their single DH counterparts (compare Figures 21a and 21b). However, in concert with calculation results presented in Figure 19b, the injection current densities corresponding to the EQE maxima are higher: around 30 and 60 A/cm^2 for the quad 3 nm and the dual 6 nm DH structures, respectively. At 200 A/cm^2, the relative EQEs retain 82% and 88% of their maxima for the quad 3 nm and the dual 6 nm DH LEDs, respectively, in reasonable agreement with calculations (Figure 14c). The hex 3 nm DH LED (Figure 21b) has the same maximum EQE value as the single and the quad 3 nm DH structures with negligible efficiency degradation, albeit its peak EQE value is shifted to higher injection current densities.

9. Anomalies needing further investigation

The turn-on voltage of the p-n junction used for InGaN based blue LEDs is about 3 eV, which is lower that the Fermi level separation in n- and p-GaN layers straddling the InGaN active region. Keep in mind that the junction quality is very high and thus the low quality argument cannot be used to account for the apparently lower than expected turn-on voltage. Another anomaly is that the expected polarization charge at heterointerfaces requires a weighing factor of anywhere from 0.3 to 0.7 in simulations to account for the experimental observation to the extent that can be delineated. Clearly one or more fundamental issues are amiss here and require a deeper investigation than that undertaken so far. It is well known from the heterojunction FET activities that no such weighing factor is needed for electrons to attain a good agreement between expectations and the experimentally determined polarization induced electron charge [102], because the salient difference between LEDs and n-channel FETs is that the former possess holes. This then suggests, naturally, that the necessity of the weighing factor has something to do with holes.

It has become a proverbial exercise in the community to assume that just because the screening of polarization requires some number of holes, those holes would somehow exist and the equilibrium would be reached. This assumption is flawed in that, while true for electrons, free holes in sufficient quantities are not available, unless injected from the p-side in requisite quantity, to induce equilibrium. With bias for example, minority carriers are injected that would affect polarization and bias induced fields and local band edge profile as well as recombination. Although the picture is very complex, we have employed the commercial Silvaco Atlas package to simulate the conduction and valence band edges with bias producing 50 A cm^{-2}, which is typical for LEDs, where the electron response for screening is set to 0% (just for completeness) and 100%, while that for holes is set to 0%, 30%, 60%, and 100%, the results of which are shown in Figure 22. The effect of holes on screening, which is similar to setting boundary conditions, is clearly seen. Without hole screening of the polarization charge a priori, the quantum well band structure indicates electron accumulation but no corresponding hole accumulation, which the electron holography mapping experimenters might be referring to as charge asymmetry.

Although very preliminary in nature, to make the point that the turn-on voltage actually depends on the screening of free carriers (hole and electrons), we show the calculated values of the same using a commercial software package (Silvaco Atlas) for an LED structure wherein 100% response from electrons is assumed but the hole response has been varied between 0% and 100% in steps. The results shown in Figure 23 are indicative of turn-on voltage being dependent on the hole response. While there is a substantial amount of additional work that must be done to make a definitive statement and there are a myriad of questions to be answered, these very preliminary data give us a glimpse into what might be responsible for lower than the expected turn-on voltage. Among the questions that arise, which is true for any software produced data, even for the measured data for that matter, is the accuracy of the results. For example, the rise in the resistance as the hole response to polarization is increased under injection is one that requires an in depth investigation. However, the point that is being made here is that long standing assumptions should no longer be automatically used and the much needed light on the underlying fundamentals must be shone.

Fortuitously, breathtaking advances in the realm of transmission electron microcopy are beginning to allow mapping of the strain in general [103,104] and in LED structures in particular [105], and composition accurately across the heterojunction. The combination of these, as determined, can be used to calculate the charge, which can be compared and contrasted to the charge mapped using electron holographic methods [106]. Specifically, dark-field inline electron holography has recently been developed to map strain in semiconductor

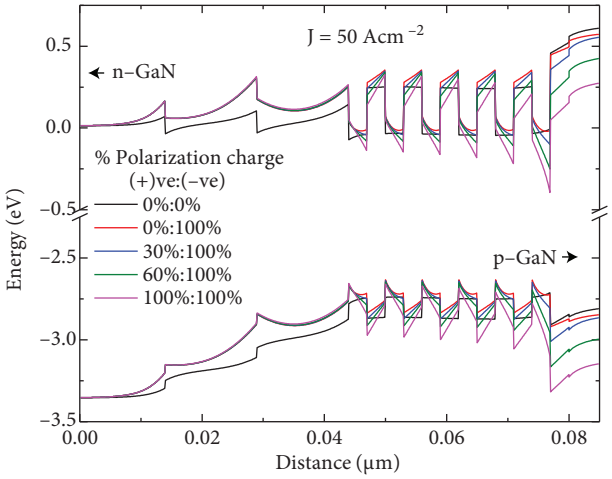

Figure 22. The conduction and valence band edges with bias producing 50 A cm $^{-2}$, which is typical for LEDs, where the electron response for screening is set to 0% (just for completeness) and 100%, while that for hole is set to 0%, 30%, 60%, and 100% for a 6 period DH LED structure with 3 nm active region thickness.

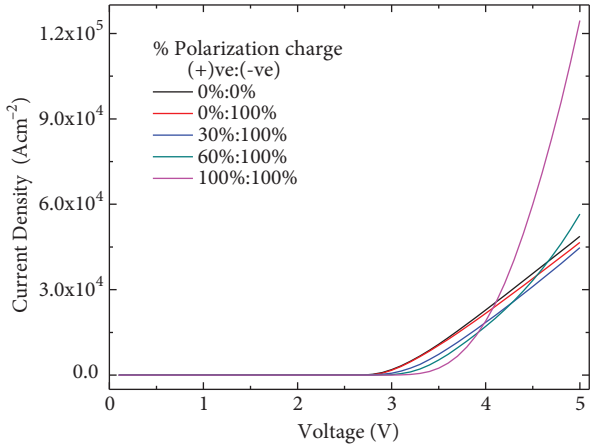

Figure 23. I-V characteristics calculated using a commercial software package (Silvaco) for artificially assumed cases of 0%, 30%, 60%, and 100% free hole response to polarization induced charge while assuming 100% response from free electrons. Note the variation in the turn-on voltage from ∼2.8 V to ∼3.8 V when the hole response to polarization charge is increased from 0% to 100%. The change in the on resistance is an issue that remains to be addressed.

heterostructures with high precision at the sub-nm spatial resolution in fields-of-view greater than 1 mm [107]. The transport-of-intensity-equation (TIE) and a flux-preserving iterative approach have been employed to reconstruct the geometric phase from a transmission electron microscopy dark-field focal series and their effects on the strain. While the TIE relies on only 3 images, optimization of 2 free parameters, namely the defocus step and low-limit cut-off frequency, is imperative. The iterative reconstruction algorithm is void of any adjustable parameter and utilizes images recorded for 9 different planes of focus with increasing, quadratic, defocus values. Very interestingly, an asymmetric distribution of internal electrostatic potential as well as an asymmetric charge distribution across the InGaN/ GaN interfaces has been noted [108]. As alluded to earlier, a wildly varying weighing factor between 0.3 and 0.7 is typically used for the polarization charge in order to attain some sort of consistency between the simulations and experiments.

To summarize this section, smaller than expected turn-on voltage is not due to poor junction quality.

Because of the abundance of electrons in the system, one would surmise that the hole screening charge might not be in equilibrium and that this is very likely to be the root cause of these apparent anomalies.

10. Conclusions

We discussed the possible origins of efficiency loss observed in InGaN LEDs under high injection, the most prevalent candidates being Auger recombination and electron overflow. There is theoretical and experimental evidence supporting both theories and the debate on the dominant contributor rages on. The LED industry, however, has been reporting internal quantum efficiencies in excess of 90% at operating current levels, which shows that the stated efficiency loss is not haunting the future of InGaN LEDs. Nevertheless, an ample discussion of both directly and indirectly deduced Auger contributions to the efficiency reduction is provided. Noting that an electron blocking layer (EBL) has been an industry standard and the electron overflow has been unequivocally shown to contribute to efficiency loss, we discussed a model describing ballistic and quasi-ballistic electron transport across InGaN active regions that results in carriers escaping to p-GaN without recombining in the active regions. The model utilizes the LO phonon scattering rates deduced from data obtained in field effect transistors, considering the electron scattering and transport in this new realm and aims to shed light on the efficiency degradation observed in InGaN LEDs. In this realm, we also elaborated on the efficacy of InGaN staircase electron injector (SEI), a structure with step-wise increased In composition, inserted before the active region for enhanced thermalization of the injected electrons to reduce the electron overflow. Unlike the EBLs commonly employed in InGaN LEDs between the p-GaN and the LED active region, which impedes the hole transport, the SEI approach does not impede hole injection into the active region. We extended our investigation to include the effects of active-region and SEI designs, which are interdependent, on the electroluminescence efficiency and efficiency degradation in LEDs based on single and multiple DHs. Owing to the 3D nature of the density of states, DH structures represent an attractive alternative to quantum wells if all else were equal. Technological considerations seem to be tilting the argument in favor of quantum wells, a term that is very liberally used even when active layer thickness is not sufficiently thin for quantization. However, the increase in DH width beyond 6 nm reduces the overlap of electron and hole wavefunctions and thus gives rise to a reduced injection-dependent effective radiative recombination coefficient.

Our findings indicate that the 2-layer SEI with optimum design significantly reduces the electron overflow by cooling the electrons before they enter the active region, and that the optimum SEI design depends on the specifics of the active region structure employed, such as composition, thickness, and number of the recombination zones. We have demonstrated that thick active regions, particularly those incorporating multiple 3 nm or 6 nm DHs separated by 3-nm $In_{0.06}Ga_{0.94}N$, naturally cool the electrons more efficiently upon injection. Thin $In_{0.06}Ga_{0.94}N$ barriers of reduced height, designed to improve hole transport across the active region, were also found to efficiently enhance cooling of ballistic and quasi-ballistic electrons within the active region.

Finally, there are some anomalies regarding the turn-on voltage, which is smaller than that expected, and some arbitrary reduction of the polarization induced charge in the active region by a factor ranging from 0.3 to 0.7. At the fundamental level it is very plausible that both may have their genesis in automatic priori assumption that there are sufficient holes in the system to screen the polarization fully.

It should be reiterated that despite the purported inherent problems related to efficiency loss discussed in this paper, one cannot overlook the fact that industry is marching along and InGaN LEDs in many forms are successfully penetrating into our lives. While the discussion is dominated by the debate between Auger recombination and electron overflow, further improvements in InGaN LED efficiency necessitates enhanced hole concentrations and efficient heat removal.

Acknowledgments

The research at VCU was funded by a grant from the Air Force Office of Scientific Research. The authors thank A Yankovich and Dr A Kvit and Prof P Voyles for STEM studies of LED structures. Extensive discussions with Prof C Weisbuch were very illuminating for general understanding of the data and his overall comments were very useful in improving the manuscript.

References

[1] Morkoç, H. *Handbook of Nitride Semiconductors and Devices*, Volume 3, Chapters 1 and 3, Wiley-VCH: Weinheim, Germany, 2008.

[2] Shim, J. I. In *III-Nitride Based Light Emitting Diodes and Applications*; Seong, T.; Han, J.; Amano, H.; Morkoç H. Eds. Springer: Dordrecht, Germany, 2013, pp. 153–195.

[3] Verzellesi, G.; Saguatti, D.; Meneghini, M.; Bertazzi, F.; Goano, M.; Meneghesso, G.; Zanoni, E. *J. Appl. Phys.* **2013**, *114*, 071101.

[4] Krames, M. R.; Shchekin, O. B.; Mueller-Mach, R.; Mueller, G. O.; Zhou, L.; Harbers, G.; Craford, M. G. *J. Display Tech.* **2007**, *3*, 160–175.

[5] Shen, Y. C.; Mueller, G. O.; Watanabe, S.; Gardner, N. F.; Munkholm, A.; Krames, M. R. *Appl. Phys. Lett.* **2007**, *91*, 141101.

[6] Delaney, T.; Rinke, P.; Van de Walle, C. G. *Appl. Phys. Lett.* **2009**, *94*, 191109.

[7] Gardner, N. F.; Müller, G. O.; Shen, Y. C.; Chen, G.; Watanabe, S. *Appl. Phys. Lett.* **2007**, *91*, 243506.

[8] Iveland, J.; Martinelli, L.; Peretti, J.; Speck, J.; Weisbuch, C. *Phys. Rev. Lett.* **2013**, *110*, 177406.

[9] Bertazzi, F.; Goano, M.; Bellotti, E. *Appl. Phys. Lett.* **2012**, *101*, 011111.

[10] Monemar, B.; Sernelius, B. E. *Appl. Phys. Lett.* **2007**, *91*, 181103.

[11] Kim, M. H.; Schubert, M. F.; Dai, Q.; Kim, J. K.; Schubert, E. F.; Piprek, J.; Park, Y. *Appl. Phys. Lett.* **2007**, *91*, 183507.

[12] Rozhansky, I. V.; Zakheim, D. A. *Phys. Status Solidi A* **2007**, *204*, 227–230.

[13] Xie, J.; Ni, X.; Fan, Q.; Shimada, R.; Özgür, Ü.; Morkoç, H. *Appl. Phys. Lett.* **2008**, *93*, 121107.

[14] Ahn, B. J.; Kim, T. S.; Dong, Y.; Hong, M. T.; Song, J. H.; Yuh, H. K.; Choi, S. C.; Bae, D. K.; Moon, Y. *Appl. Phys. Lett.* **2012**, *100*, 031905.

[15] Hader, J.; Moloney, J. V.; Koch, S. W. *Appl. Phys. Lett.* **2010**, *96*, 221106.

[16] Cao, X. A.; Yang, Y.; Guo, H. *J. Appl. Phys.* **2008**, *104*, 093108.

[17] Efremov, A. A.; Bochkareva, N. I.; Gorbunov, R. I.; Larinovich, D. A.; Rebane, Y. T.; Tarkhin, D. V.; Shreter, Y. G. *Semicon.* **2006**, *40*, 605–610.

[18] Ni, X.; Li, X.; Lee, J.; Liu, S.; Avrutin, V.; Özgür, Ü.; Morkoç, H.; Matulionis, A.; Paskova, T.; Mulholland, G.; Evans, K. R. *Appl. Phys. Lett.* **2010**, *97*, 031110.

[19] Piprek, J. *Phys. Status Solidi (a)* **2010**, *207*, 2217–2225.

[20] Hader, J.; Moloney, J. V.; Pasenow, B.; Koch, S. W.; Sabathil, M.; Linder, N.; Lutgen, S. *Appl. Phys. Lett.* **2008**, *92*, 261103.

[21] David, A.; Gardner, N. F. *Appl. Phys. Lett.* **2010**, *97*, 193508.

[22] Laubsch, A.; Sabathil, M.; Bergbauer, W.; Strassburg, M.; Lugauer, H.; Peter, M.; Lutgen, S.; Linder, N.; Streubel, K.; Hader, J.; et al. *Phys. Status Solidi C* **2009**, *6*, 913–916.

[23] David, A.; Grundmann, M. J. *Appl. Phys. Lett.* **2010**, *96*, 103504.

[24] Chen, G.; Craven, M.; Kim, A.; Munkholm, A.; Watanabe, S.; Camras, M.; Götz, W.; Steranka, F. *Phys. Status Solidi A* **2008**, *205*, 1086–1092.

[25] Bulashevich, K. A.; Karpov, S. Y. *Phys. Status Solidi C* **2008**, *5*, 2066–2069.

[26] Ryu, H. Y.; Kim, H.; Shim, J. *Appl. Phys. Lett.* **2009**, *95*, 081114.

[27] Laubsch, A.; Sabathil, M.; Baur, J.; Peter, M.; Hahn, B. *IEEE Trans. Electron Devices* **2010**, *57*, 79–87.

[28] Ryu, H. Y.; Choi, W. J.; Jeon, K. S.; Kang, M. G.; Choi, Y.; Lee, J. S. *J. Appl. Phys.* **2012**, *112*, 083109.

[29] Bertazzi, F.; Goano, M.; Bellotti, E. *Appl. Phys. Lett.* **2010**, *97*, 231118.

[30] Kioupakis, E.; Rinke, P.; Delaney, K. T.; Van de Walle, C. G. *Appl. Phys. Lett.* **2011**, *98*, 161107.

[31] Heinemann, M.; Heiliger , C. *J. Appl. Phys.* **2011**, *110*, 083103.

[32] Galler, B.; Drechsel, P.; Monnard, R.; Rode, P.; Stauss, P.; Froehlich, S.; Bergbauer, W.; Binder, M.; Sabathil, M.; Hahn, B.; et al. *Appl. Phys. Lett.* **2012**, *101*, 131111.

[33] Schiavon, D.; Binder, M.; Peter, M.; Galler, B.; Drechsel, P.; Scholz, F. *Phys. Status Solidi (b)* **2013**, *250*, 283–290.

[34] Dyakonov, M. I.; Kachorovskii, V. Y. *Phys. Rev. B* **1994**, *17*, 130–138.

[35] Andreev, A. D.; Zegrya, G. G. *Semiconductors* **1997**, *31*, 297–303.

[36] Gilard, O.; Lozes-Dupuy, F.; Vassilieff, G.; Barrau, J.; Jeune, P. *J. Appl. Phys.* **1998**, *84*, 2705–2715.

[37] Polkovnikov, A. S.; Zegrya, G. G. *Phys. Rev. B* **1998**, *58*, 4039–4056.

[38] Andreev, A. D.; O'Reily, E. P. *Appl. Phys. Lett.* **2004**, *84*, 1826–1828.

[39] Hader, J.; Moloney, J. V.; Koch, S. W. *IEEE J. Quantum Electron.* **2005**, *41*, 1217–1226.

[40] Vaxenburg, R.; Lifshitz, E.; Efros, A. L. *Appl. Phys. Lett.* **2013**, *102*, 031120.

[41] Vaxenburg, R.; Rodina, A.; Lifshitz, E.; Efros, A. L. *Appl. Phys. Lett.* **2013**, *103*, 221111.

[42] Bertazzi, F.; Zhou, X.; Goano, M.; Ghione, G.; Bellotti, E. *Appl. Phys. Lett.* **2013**, *103*, 081106.

[43] Wu, S.; Geiser, P.; Jun, J.; Karpinski, J.; Wang, D.; Sobolewski, R. *J. Appl. Phys.* **2007**, *101*, 043701.

[44] Peretti, J.; Weisbuch, C.; Iveland, J.; Piccardo, M.; Martinelli, L.; Speck, J. S. In *Conference Proceedings: "Light-Emitting Diodes: Materials, Devices, and Applications for Solid State Lighting XVIII", SPIE OptoWest Symposium*, February 3–6, San Francisco CA, USA, 2014, vol. 9003, p. 90030Z-1.

[45] Piccardo, M.; Martinelli, L.; Iveland, J.; Young, N.; DenBaars, S. P.; Nakamura, S.; Speck, J. S.; Weisbuch, C.; Peretti, J. *Phys. Rev. B* **2014**, *89*, 235124.

[46] Cobet, C.; Goldhahn, R.; Richter, W.; Esser, N. *Phys. Status Solidi B* **2009**, *246*, 1440–1449.

[47] Feneberg, M.; Romero, M. F.; Röppischer, M.; Cobet, C.; Esser, N.; Neuschl, B.; Thonke, K.; Bickermann, M.; Goldhahn, R. *Phys. Rev. B* **2013**, *87*, 235209.

[48] de Carvalho, L. C.; Schleife, A.; Furthmüller, J.; Bechstedt, F. *Phys. Rev. B* **2013**, *87*, 195211.

[49] Bellotti, E.; Bertazzi, F.; Shishehchi, S.; Matsubara, M.; Goano, M. *IEEE Trans. Electron Dev.* **2013**, *60*, 3204–3215.

[50] Bertazzi, F.; Moresco, M.; Bellotti, E. *J. Appl. Phys.* **2009**, *106*, 063718.

[51] Yamakawa, S.; Aboud, S.; Saraniti, M.; Goodnick, S. M. *Semicon. Sci. Tech.* **2004**, *19*, 475–477.

[52] Bertazzi, F.; Moresco, M.; Bellotti, E. *J. Appl. Phys.* **2009**, *106*, 063718.

[53] Svane, A.; Christensen, N. E.; Gorczyca, I.; van Schilfgaarde, M.; Chantis, A. N.; Kotani, T. *Phys. Rev. B* **2010**, *82*, 115102.

[54] de Carvalho, L. C.; Schleife, A.; Bechstedt, F. *Phys. Rev. B* **2011**, *84*, 195105.

[55] Albrecht, J. D.; Wang, R. P.; Ruden, P. P.; Farahmand, M.; Brennan, K. F. *J. Appl. Phys.* **1998**, *83*, 4777–4781.

[56] Semenenko, M.; Yilmazoglu, O.; Hartnagel, H. L.; Pavlidis, D. *J. Appl. Phys.* **2011**, *109*, 023703.

[57] Sun, C. K.; Huang, Y. L.; Keller, S.; Mishra, U.; DenBaars, S.; *Phys. Rev. B* **1999**, *59*, 13535–13538.

[58] Fritsch, D.; Schmidt, H.; Grundmann, M. *Phys. Rev. B.* **2003**, *67*, 235205.

[59] Goldhahn, R. private communication.

[60] Mickevicius, J.; Tamulaitis, G.; Shur, M.; Shatalov, M.; Yang, J.; Gaska, R. *Appl. Phys. Lett.* **2012**, *101*, 211902.

[61] Mickevicius, J.; Jurkevicius, J.; Shur, M. S.; Yang, J. W.; Gaska, R.; Tamulaitis, G. *Optics Exp.* **2012**, *20*, 25195–25200.

[62] Binder, M.; Nirschl, A.; Zeisel, R.; Hager, T.; Lugauer, H. J.; Sabathil, M.; Bougeard, D.; Wagner, J.; Galler, B. *Appl. Phys. Lett,* **2013**, *103*, 071108.

[63] Hader, J.; Moloney, J. V.; Koch, S. W. In *Conference Proceedings: "Light-Emitting Diodes: Materials, Devices, and Applications for Solid State Lighting XVIII", SPIE OptoWest Symposium*, San Francisco CA, USA, February 3–6, 2014, vol. 9003, p. 900336.

[64] Lee, J.; Li, X.; Ni, X.; Özgür, Ü.; Morkoç, H.; Paskova, T.; Mulholland, G.; Evans, K. R. *Appl. Phys. Lett.* **2009**, *95*, 201113.

[65] Ni, X.; Fan, Q.; Shimada, R.; Özgür, Ü.; Morkoç, H. *Appl. Phys. Lett.* **2008**, *93*, 171113.

[66] Özgür, Ü.; Liu, H.; Li, X.; Ni, X.; Morkoç, H. *Proc. IEEE* **2010**, *98*, 1180–1196.

[67] Lee, J.; Eliseev, P. G.; Osiński, M.; Lee, D. S.; Florescu, D. I.; Pophristić, M. *IEEE J. Sel. Top. Quant. Electron.* **2003**, *9*, 1239–1245.

[68] Eliseev, P. G.; Lee, J.; Osinski, M. *Quant. Electron.* **2004**, *34*, 1127–1132.

[69] Świetlik, T.; Franssen, G.; Wiśniewski, P.; Krukowski, S.; Łepkowski, S. P.; Marona, L.; Leszczyński, M.; Prystawko, P.; Grzegory, I.; Suski, T.; et al. *Appl. Phys. Lett.* **2006**, *88*, 071121.

[70] Ishibashi, T. *IEEE Trans. Electron. Dev.* **2001**, *48*, 2595–2605.

[71] Lin, G. B.; Meyaard, D.; Cho, J.; Schubert, E. F.; Shim, H. W.; Sone, C. S. *Appl. Phys. Lett.* **2012**, *100*, 161106.

[72] Ni, X.; Li, X.; Lee, J.; Liu, S.; Avrutin, V.; Özgür, Ü.; Morkoç, H.; Matulionis, A. *J. Appl. Phys.* **2010**, *108*, 033112.

[73] Ni, X.; Li, X.; Lee, J.; Liu, S.; Avrutin, V.; Matulionis, A.; Özgür, Ü.; Morkoç, H. *Superlattices and Microstructures* **2010**, *48*, 133–153.

[74] Özgür, Ü.; Ni, X.; Li, X.; Lee, J.; Liu, S.; Okur, S.; Avrutin, V.; Matulionis, A.; Morkoç, H. *Semicon. Sci. Technol.* **2011**, *26*, 014022.

[75] Tsen, K. T.; Joshi, R. P.; Ferry, D. K.; Botchkarev, A.; Sverdlov, B.; Salvador, A.; Morkoç, H. *Appl. Phys. Lett.* **1996**, *68*, 2990–2992.

[76] Ryu, H. Y.; Lee, S. H. *J. Korean Phys. Soc.* **2012**, *61*, 1395.

[77] Park, S. H.; Moon, Y. T.; Han, D. S.; Park, J. S.; Oh, M. S.; Ahn, D. *Semicond. Sci. Technol.* **2012**, *27*, 115003.

[78] Akasaka, T.; Gotoh, H.; Saito, T.; Makimoto, T. *Appl. Phys. Lett.* **2004**, *85*, 3089–3091.

[79] Huang, C.; Liu, T.; Lu, Y.; Shiao, W.; Chen, Y.; Wang, J.; Lu, C.; Yang, C. C. *J. Appl. Phys.* **2008**, *104*, 123106.

[80] Li, X.; Okur, S.; Zhang, F.; Avrutin, V.; Özgür, Ü.; Morkoç, H.; Hong, S. M.; Yen, S. H.; Hsu, T. S.; Matulionis, A. *J. Appl. Phys.* **2012**, *111*, 063112.

[81] Li, X.; Zhang, F.; Okur, S.; Avrutin, V.; Liu, S. J.; Özgür, Ü.; Morkoç, H.; Hong, S. M.; Yen, S. H.; Hsu, T. S.; Matulionis, A. *Phys. Status Solidi A* **2011**, *208*, 2907–2912.

[82] Huang, S. J.; Su, Y. K.; Tseng, C. Y.; Lin, S. C.; Hsu, H. C. *Appl. Phys. Express* **2010**, *3*, 122106.

[83] Onomura, M. In *Conference Proceedings: "Gallium Nitride Materials and Devices IX" SPIE OptoWest Symposium*, San Francisco CA, USA, February 3–6, 2014, vol. 8986, p. 898620.

[84] Yankovich, A. B.; Kvit, A. V.; Li, X.; Zhang, F.; Avrutin, V.; Liu, H. Y.; Izyumskaya, N.; Özgür, Ü.; van Leer, B.; Morkoç, H.; Voyles, P. M. *Microsc. Microanal.* **2014**, 20, 864–868.

[85] Liberis, J.; Matulionienė, I.; Matulionis, A.; Ramonas, M.; Eastman, L. F. In: *Advanced Semiconductor Materials and Devices Research: III-Nitrides and SiC*; Cha, H.-Y., Ed. Transworld Research Network: Kerala, India, 2009.

[86] Dai, Q.; Shan, Q. F.; Cho, J. H.; Schubert, E. F.; Crawford, M. H.; Koleske, D. D.; Kim, M. H.; Park, Y. *App. Phys. Lett.* **2011**, *98*, 033506.

[87] Ščajev, P.; Jarašiūnas, K.; Okur, S.; Özgür, Ü.; Morkoç, H. *J. Appl. Phys.* **2012**, *111*, 023702.

[88] Im, J. S.; Kollmer, H.; Off, J.; Sohmer, A.; Sholz, F.; Hangleiter, A. In *Proceeding of Materials Research Society Symposium, Nitride Semiconductors*, December 1–3, 1997, Boston MA, USA, 1997, vol. 482, p. 513.

[89] Perlin, P.; Kisielowski, C.; Iota, V.; Weinsten, B. A.; Mattos, L.; Shapiro, N. A.; Kruger, J.; Weber, E. R.; Yang, J. *Appl. Phys. Lett.* **1998**, *73*, 2778–2780.

[90] Ambacher, O.; Majewski, J.; Miskys, C.; Link, A.; Hermann, M.; Eickhoff, M.; Stutzmann, M.; Bernardini, F.; Fiorentini, V.; Tilak, V.; Schaff B.; Eastman, L. F. *J. Phys.: Condens. Matter* **2002**, *14*, 3399–3434.

[91] Blood, P. *IEEE J. Quantum Elec.* **2000**, *36*, 354–362.

[92] Litvinov, V. I. *J. Appl. Phys.* **2000**, *88*, 5814–5820.

[93] Radtke, R. J.; Waghmare, U.; Ehrenreich, H.; Grein, C. H. *Appl. Phys. Lett.* **1998**, *73*, 2087–2089.

[94] Dmitriev, A.; Oruzheinikov, A. *J. Appl. Phys.* **1999**, *86*, 3241–3246.

[95] Sala, D.; Di Carlo, A.; Lugli, P.; Bernardini, F.; Fiorentini, V.; Scholz, R.; Jancu, J. M. *Appl. Phys. Lett.* **1999**, *74*, 2002–2004.

[96] Dai, Q.; Schubert, M. F.; Kim, M. H.; Kim, J. K.; Schubert, E. F.; Koleske, D. D.; Crawford, M. H.; Lee, S. R.; Fischer, A. J.; Thaler, G.; et al. *Appl. Phys. Lett.* **2009**, *94*, 111109.

[97] Wang, L.; Liu, C.; Lu, J. N.; Liu, L.; Liu, N. Y.; Chen, Y. J.; Zhang, Y. F.; Gu, E. D.; Hu, X. D. *Optics Express* **2011**, *19*, 14182–14187.

[98] David, A.; Grundmann, M. J.; Kaeding, J. F.; Gardner, N. F.; Mihopoulos, T. G.; Krames, M. R. *Appl. Phys. Lett.* **2008**, *92*, 053502.

[99] Liu, J. P.; Ryou, J. H.; Dupuis, R. D.; Han, J.; Shen G. D.; Wang, H. B. *Appl. Phys. Lett.* **2008**, *93*, 021102.

[100] Zhu, J. H.; Zhang, S. M.; Wang, H.; Zhao, D. G.; Zhu, J. J.; Liu, Z. S.; Jiang, D. S.; Qiu, Y. X.; Yang, H. *J. Appl. Phys.* **2011**, *109*, 093117.

[101] Li, X.; Okur, S.; Zhang, F.; Hafiz, S. A.; Avrutin, V.; Özgür, Ü.; Morkoç, H.; Jarasiunas, K. *App. Phys. Lett.* **2012**, *101*, 041115.

[102] See for example: Morkoç, H. *Nitride Semiconductor Devices: Fundamentals and Applications*, Wiley VCH: Weinheim, Germany, 2013.

[103] Koch, C. T.; Ozdol, V. B.; van Aken, P. A. *Appl. Phys. Lett.* **2010**, *96*, 091901.

[104] Ozdol, V. B.; Koch, C. T.; van Aken, P. A. *J. Appl. Phys.* **2010**, *108*, 056103.

[105] Song, K.; Shin, G. Y.; Kim, J. K.; Oh, S. H.; Koch, C. T. *Ultramicroscopy* **2013**, *127*, 119–125.

[106] Oh, S. H.; In *Conference Proceedings: "Gallium Nitride Materials and Devices IX" SPIE OptoWest Symposium*, San Francisco CA, USA, February 3–6, 2014, vol. 8986, p. 8986-17.

[107] Song, K.; Koch, C. T.; Shin, G. Y.; Kim, J. K.; Oh, S. H. *In Conference Proceedings: APMC 10/ICONN 2012/ACMM 22*, Perth, Western Australia, February 5–9, 2012, p. 924.1–924.2.

[108] Lee, J. K.; Song, K.; Jung, W. Y.; Kim, J. K.; Park, C. G.; Oh, S. H. In *Conference Abstracts: 10th International Conference on Nitride Semiconductors 2013 (ICNS-10),* Washington DC, USA, August 25–30, 2013.